TUDelft

Delft University of Technology

Roles of the grain-boundary characteristics and distributions on hydrogen embrittlement in face-centered cubic medium-entropy $V_xCr_{1-x}CoNi$ alloys

Yang, Dae Cheol; Song, Sang Yoon; Kim, Han Jin; Lee, Sang In; Dutta, Biswanath; Kim, Young Kyun; Shim, Jae Hyeok; Suh, Jin Yoo; Na, Young Sang; Sohn, Seok Su

Important note
To cite this publication, please use the final published version (if applicable).
Please check the document version above.

Roles of the grain-boundary characteristics and distributions on hydrogen embrittlement in face-centered cubic medium-entropy $V_xCr_{1-x}CoNi$ alloys

Dae Cheol Yang [a], Sang Yoon Song [a], Han-Jin Kim [b], Sang-In Lee [b], Biswanath Dutta [c], Young Kyun Kim [d], Jae-Hyeok Shim [b,e], Jin-Yoo Suh [b], Young Sang Na [d,*], Seok Su Sohn [a,**]

[a] Department of Materials Science and Engineering, Korea University, 02841, Seoul, Republic of Korea
[b] Energy Materials Research Center, Korea Institute of Science and Technology, 02792, Seoul, Republic of Korea
[c] Department of Materials Science and Engineering, Faculty of Mechanical, Maritime and Materials Engineering, Delft University of Technology, Mekelweg 2, 2628 CD, Delft, the Netherlands
[d] Department of Special Alloys, Extreme Materials Research Institute, Korea Institute of Materials Science, 51508, Changwon, Republic of Korea
[e] KIST-SKKU Carbon-Neutral Research Center, Sungkyunkwan University (SKKU), 16419, Suwon, Republic of Korea

ABSTRACT

The issue of hydrogen embrittlement (HE) in face-centered (FCC) structured alloys is significant for H storage and transportation application due to unanticipated damage beyond its predicted service life. This unpredictable situation may harm human life and limit hydrogen to a reliable source of renewable energy in industrial fields. Recent research has suggested that multi-principal element alloys possess high resistance to HE. However, there has been limited exploration of how their unique properties affect the HE mechanisms. In this study, using simple model VCrCoNi alloys with analogous grain sizes, the reduction rate of ductility by hydrogen uptake was measured through a slow strain rate tensile test following electro-chemical H charging. Further, the origin of HE resistance was investigated by analyzing various factors such as hydrogen contents, fracture and deformation behaviors, and grain boundary properties using thermal desorption spectroscopy, scanning electron microscope, and electron backscatter diffraction. Despite the consistent trends of the H content, stacking fault energy, and stress with increasing V content, the resistance to HE is the highest for the alloy with an intermediate ratio of V and Cr, namely, for the $V_{0.7}Cr_{0.3}CoNi$ alloy. Through the analysis of grain boundary characteristics, the high resistance is attributed to large fractions of special boundaries and special triple junctions and large twin-related domain size, which suppresses crack growth and interlinkage. The favorable grain boundary characteristics result from mechanical dynamic recovery, achieved by the competitive effects of solid-solution strengthening and stacking fault energy. Thus, the present study provides novel insights into enhancing HE resistance in FCC-structured alloys.

1. Introduction

Hydrogen (H) is currently receiving considerable interest as a sustainable energy source for the future, and there are various methods for its storage and transportation. Among the various types of use, liquid hydrogen (LH2) is advantageous due to its high volumetric energy density and requirement for less storage space [1]. However, metal containers used for LH2 storage are susceptible to hydrogen embrittlement (HE) environments, which weaken ductile properties and lead to premature destruction owing to interactions between H and various microstructural defects [2–6]. In addition, LH2, which must be cooled to ultra-low temperatures and maintained in a fully liquid state at atmospheric pressure, also requires resistance to cryogenic embrittlement. Consequently, exposure to these extreme environmental conditions may result in the brittleness of material and subsequent leakage of H, thereby leading to catastrophic accidents. Therefore, it is crucial to develop materials with exceptional resistance to hydrogen and cryogenic embrittlement, which can be used to store and transport H safely. Accordingly, materials used for LH2 storage should possess two characteristics to prevent both H and cryogenic embrittlement [7,8]: (1)

face-centered cubic (FCC) phase alloy systems with low H diffusivity, and (2) no secondary and precipitate phases that cause a ductile–brittle transition at cryogenic temperatures. In this regard, thermomechanically stable FCC single-phase alloys are suitable for these extreme conditions; particularly, 316L stainless steel is perceived as a typical example [9].

Numerous studies on the HE resistance of existing stable FCC single-phase alloys have been performed mainly based on plastic deformation and stacking fault energy (SFE) [10–16]. Dislocation-mediated plasticity occurs primarily in high-SFE alloys ($\gamma_{SFE} \geq \sim 40$ mJ m^{-2}), in which only the interaction between H-induced dislocation glides and GBs can induce HE [10–12]. However, deformation twins occur in low-SFE alloys ($\gamma_{SFE} \leq \sim 40$ mJ m^{-2}), and these twins critically interact with H. According to previous reports [13,17], such twins either prohibit or accelerate the propagation of H-induced intergranular cracks, depending on the fraction of coherent and incoherent twins and the arrangement of the relative directions of cracks and twins. HE does not occur solely owing to the presence of H but rather by the interaction of H and microstructural defects. Therefore the variation in SFE must be considered as it significantly affects deformation behaviors, trap sites, and consequent H-induced fracture [13–15].

Multi-principal element alloys (MPEAs), also known as high- or medium-entropy alloys (HEAs or MEAs), have recently received considerable attention owing to their superior mechanical, chemical, and functional properties [17–23]. Variations in deformation behavior according to SFE are also applicable in FCC single-phase MPEAs, similar to existing dilute FCC alloys. However, these alloys are distinguished from existing alloys by severe lattice distortion and the presence of multi-principal elements that embody each intrinsic characteristic to a certain extent. This atomic-scale structural change in MPEAs may disperse energy barriers against H diffusion and trapping [24], and new research with a different perspective should be conducted, unlike the already studied FCC alloys; however, no related practical studies have yet been reported. To control solid-solution strengthening, Wu et al. [25] investigated several equiatomic binary, ternary, and quaternary FCC alloys in which alloying elements, such as Cr, Mn, Fe, and Co, were added to pure Ni. However, alloying several multi-principal elements with similar fractions is unsuitable for elucidating the interaction between solid-solution strengthening and H alone. This is because the behavior of H is affected by not only the structural influence but also the chemical affinity among elements.

To better understand these interactions, we select the V$_x$Cr$_{1-x}$CoNi MEA systems as model alloys. First, as previously reported [26], the solid-solution strengthening and SFE could be dramatically controlled in these model alloys by adjusting the V/Cr ratio between CrCoNi and VCoNi alloys, which possess thermomechanically stable FCC single-phase structures. This regulation provides insights into the interplay between distinctive characteristics of MPEAs and hydrogen. Second, the chemical effect of each element on the affinity of H can be minimized in these alloy systems by maintaining the exact composition of Co and Ni and by controlling only the V/Cr ratio, although it is challenging to completely neglect the chemical effect.

In addition to solid-solution strengthening and SFE, GB characteristics should be considered, as the GBs are the primary sites for HE and intergranular fracture in FCC-structured alloys. Special boundaries (SBs) whose cohesive strengths are greater than those of random boundaries can resist the intergranular cracking caused by HE, liquid metal embrittlement, and intergranular corrosion [27–32]. Therefore, the fraction of SBs has been controlled through specific thermomechanical treatments, known as grain boundary engineering (GBE), in several previous studies. However, GB characteristics could also be modified in response to changes in the intrinsic properties, such as solid-solution strengthening and SFE [33,34]. These modifications can significantly affect the HE resistance of the proposed model alloys in which solid-solution strengthening and SFE are varied simultaneously.

In this respect, this study aims to unravel the effect of solid-solution

strengthening and SFE on the HE mechanisms in V$_x$Cr$_{1-x}$CoNi MEAs with a tailored V/Cr ratio. H was precharged by electrochemical cathodic charging, and the precharged H content and its interaction with microstructural defects were quantitatively analyzed using thermal desorption analysis (TDA). HE susceptibility was evaluated using slow strain rate tensile (SSRT) tests, and the resulting deformation behaviors, fracture appearances, and H-induced crack development under stepwise tensile strains were investigated. These systematic investigations revealed that the HE susceptibility was predominantly affected by GB characteristics in terms of the SBs, special triple junctions (STJs), and twin-related domains (TRDs). We revealed that the controlled variables, *i.e.*, solid-solution strengthening and SFE with the V content, are closely correlated with GB characteristics rather than directly altering the HE mechanism. This finding provides novel insights into the improvement of the HE resistance of highly concentrated MPEAs.

2. Experimental methods

2.1. Alloy fabrications

As mentioned above, we selected the alloys with the controlled V/Cr ratio to investigate the interaction between the atomic-scale structural change and hydrogen. Four V$_x$Cr$_{1-x}$CoNi (x = 0, 0.4 0.7, and 1) alloys (180 g) were produced using a vacuum induction melting technique (model: MC100V, Indutherm, Walzbachtal–Wössingen, Germany). To manufacture ingots (length × width × thickness: 80 × 35 × 8 mm^3), high-purity elements of 99.95% were stacked in a zirconia crucible and then cast in a graphite mold. Before the graphite mold was placed in a furnace, it was preheated to 100 °C for 0.5 h to remove water vapor. Prior to melting, the melting furnace chamber was evacuated to a pressure of 6×10^{-2} Pa and refilled with high-purity Ar gas until the pressure reached 6×10^4 Pa. This cleaning process was repeated five times to prevent the mixing of the impurity gas. The cast ingots were homogenized at 1150 °C for 2 h in a tube furnace under an Ar atmosphere and then water-quenched, followed by cold-rolling to achieve a thickness reduction. The flat rolling process is used to reduce the thickness of a plate-shaped ingot using two 50 cm-diameter rolls. This process involves the insertion of the ingot between two rolls that are independently driven and rotated to compress the material. The roll was operated at a speed of 3.0 rpm, and the desired reduction in thickness of 80% was achieved by decreasing the roll gap from 7 mm to 0.5 mm. The 1.5-mm-thick cold-rolled sheets were annealed in an Ar atmosphere and quenched with water. The annealing was conducted for 10 min, and temperatures were determined to be 880 °C for CrCoNi and (V$_{0.4}$Cr$_{0.6}$)CoNi, 910 °C for (V$_{0.7}$Cr$_{0.3}$)CoNi, and 930 °C for VCoNi to produce a similar grain size of approximately 5 μm for the four alloys.

2.2. Hydrogen pre-charging and TDA

Hydrogen was electrochemically pre-charged in the electrolyte using a cathodic charging method. The Pt electrode was used as an anode, and the alloys served as cathodes for hydrogen generation. A mixture of 0.5 M H$_2$SO$_4$ was employed as the charging solution with 5 g/L thiourea as a recombination poison, and charging was conducted at a consistent current density of 50 mA cm^{-2} for 24 h. All the specimens were polished with 400, 800, 1200, 2000, and 4000 grit SiC papers to minimize their surface roughness and induce hydrogen uniformly. After H pre-charging was completed, the specimens were cleaned with distilled water and ethanol and then dried using a dryer.

TDA was performed to measure the H content and analyze the H-trapping behavior using a hot extraction analyzer (G4 Phoenix, Bruker, Germany) equipped with a thermal conductivity detector for plate-type specimens (size: 20 × 30 × 1 mm^3). The initial step was to examine the four alloys up to 800 °C, confirming the absence of a high-temperature peak above 400 °C. Thus, the consistency of the H levels was confirmed by repeating the analysis 4–7 times from the ambient temperature to

400 °C using gaseous nitrogen as the carrier gas that transports desorbed hydrogen into the analyzer. Gaseous nitrogen is used as a carrier gas to determine hydrogen content because of the relatively large difference in thermal conductivity. The desorbed H was determined by calculating the area within the resultant curves. TDA was performed at the three different heating rates of 200, 300, and 400 °C h^{-1} to investigate the activation energy (E_a) associated with various defects for H desorption and diffusion. E_a was calculated as a function of the peak temperature of each hydrogen desorption curve using the Kissinger equation [35],

$$\ln\left(\frac{\beta}{T_p^2}\right) = -\frac{E_a}{RT_p} \tag{1}$$

where β, T_p, and R indicates the heating rates, peak temperature of hydrogen desorption curves in each heating rate, and gas constant (8.314 kJ mol^{-1}), respectively.

2.3. Mechanical tests

Dog-bone-shaped plate specimens (gage length × width × thickness: 12 × 2.5 × 1.5 mm^3) were prepared via electrical discharge machining. Uniaxial tensile tests were performed using a universal testing machine (Model 8801, Instron, USA) with a crosshead speed of 1 × 10^{-4} s^{-1} at room temperature (298 K). The SSRT tests ensure that H interacts sufficiently with dislocations that glide during plastic deformation [36]. The degree of HE was quantified based on the loss of tensile elongation using the hydrogen embrittlement index (HEI), as follows:

$$\text{HEI} = \frac{El_{uncharged} - El_{charged}}{El_{uncharged}} \times 100 \tag{2}$$

where $El_{uncharged}$ and $El_{charged}$ denote the total elongations of the specimens before and after H charging, respectively. Particularly for the H pre-charged specimens, the specimen thickness should be consistent throughout all the test specimens because it affects the proportion of the H-charged zone in each specimen. A large variance in the proportion can cause the degree of HE to fluctuate. The thickness of 1.5 mm was precisely regulated at the final polishing step, and the thickness variation was kept to a minimum. The proportion of the H-charged zone was controlled within a deviation of 5%.

2.4. Microstructural analysis

The grain size and morphology of the FCC phase were investigated via electron backscatter diffraction (EBSD). The final mechanical polishing was conducted using a colloidal silica suspension for 0.5 h to remove damaged layers formed by cutting and grinding. EBSD analysis was performed using field-emission scanning electron microscopy (FE-SEM, Hitachi, S-4300SE, Japan) in conjunction with an EDAX data collection system and TSL OIM Analysis™ v8 software. The lattice parameters were characterized using X-ray diffraction (XRD, D Max 2500, Rigaku, Japan) with Cu K-α radiation. The scans were performed from 20° to 100° at a scan rate of 5° min^{-1} with a step size of 0.02°.

Hydrogen-induced brittle cracks were investigated with respect to crack initiation and propagation from the surface to the interior in the transverse direction (TD) plane. The crack paths and morphology near the surface and the resulting fracture surfaces of the tensile specimens were examined using FE-SEM (Quanta FEG 250, FEI, USA). In each fractograph of the TD planes, 2–3 cracks with the largest area and sufficient depth were defined as "major cracks." Statistical data for the number, depth and width of the cracks were determined using the commercial ImagePro software. In the dataset, the number of cracks decreased drastically to approximately one-third at 5 μm in all four alloys, and this point was considered to be an inflection point at which cracks with insufficient depth evolved into major cracks. Cracks with a depth of less than 5 μm were designated as "minor cracks" to describe

the crack growth process.

The open Python software, Pythorient, was used to identify coincidence site lattice (CSL) Σ boundaries and triple junctions. This software program is useful for characterizing the microstructure of GB engineered materials [33]. Data cleaning was performed in advance to remove the non-indexed points in the OIM software. Only EBSD measurements deemed adequate (*i.e.*, less than 10% of the data points changed with the cleaning algorithm) were used to ensure data quality. Pythorient reads the HexGrid files, which were cleaned and exported from the OIM software. By default, these data files contain phi1, Phi, phi2, x, y, image quality (IQ), confidence index (CI), fit, index (ID) of grain, and phase. The tolerance for identifying Σ3 GB was set to 8.66°, and that for identifying Σ9 GB was set to 5°. This tolerance was calculated using the Brandon criterion 15° Σ$^{-1/2}$, where Σ is the ratio of the primitive CSL unit cell volume to the primitive crystal unit cell volume, and 15° corresponds to the commonly accepted transition point between the dislocation-mediated low-angle GBs and the high-angle GBs [37].

A TRD is a cluster of twin-related grains that all have Σ3^n misorientations. ARPGE software was used to analyze the EBSD map data subjected to the same cleaning process as described above to confirm the size of the TRD in the initial microstructure. This program can reconstruct the TRD automatically using grains connected by CSL Σ ≤ 29 boundaries [38]. In addition, it is useful for quantifying the level of multiple twinning that occurs in FCC alloys through the standards of TRD size and the number of grains (N_g).

3. Results

3.1. Microstructure of annealed single FCC MEAs

Fig. 1a$_1$–d$_1$ shows the EBSD inverse pole figure (IPF) maps of cold-rolled and recrystallized CrCoNi, (V$_{0.4}$Cr$_{0.6}$)CoNi, (V$_{0.7}$Cr$_{0.3}$)CoNi, and VCoNi alloys, respectively. All the alloys had a similar grain size in the range of 5–6 μm, and the lengths of the GBs for each alloy were also almost identical at 0.85, 0.83, 0.83, and 0.81 mm, respectively, per an area of 0.01 mm^2. Thus, it is expected that the susceptibility of intergranular fracture would not be affected by the grain size and GB length. The four aforementioned alloys are referred to as V0, V40, V70, and V100, respectively, according to the V content for convenience hereafter.

3.2. SSRT properties before and after cathodic H charging

Fig. 2a–d shows the SSRT results of the four alloys before and after H pre-charging. With increasing V content, the yield strength increased in the order of 422, 585, 672, and 843 MPa, and the tensile strength also increased in the order of 860, 995, 1104, and 1267 MPa. The improvement in both the yield and tensile strengths with increasing V content resulted from the enhanced lattice friction stress and the solid-solution strengthening effect [26]. The measured HEI, which represents the rate of loss in the ductility of the specimen after hydrogen charging, increased from 5.8% to 8.4% with increasing V content, whereas HE was almost negligible for V70 (Table 1).

Although the overall HEI increased with increasing V content, the HE resistance also depended on the strength. Stronger alloys with higher stress levels are more vulnerable to HE [39]. Thus, it is reasonable to compare the resistance to HE by normalizing the HEI to the yield strength. The normalized HEIs of V0, V40, and V100 were 0.014%/MPa, 0.011%/MPa, and 0.010%/MPa, respectively, indicating that the HE susceptibility rather decreases with increasing V content, although the HEI was larger for V100 than for V0. Soundararajan et al. and Luo et al. respectively reported that V0 and V100 exhibited outstanding resistances to HE in independent studies [17,22]. However, the present study confirms that V100 shows higher resistance to HE compared with V0 when considering a higher strength for similar grain size. Interestingly, V70 has the highest resistance to HE among the VCrCoNi MEAs
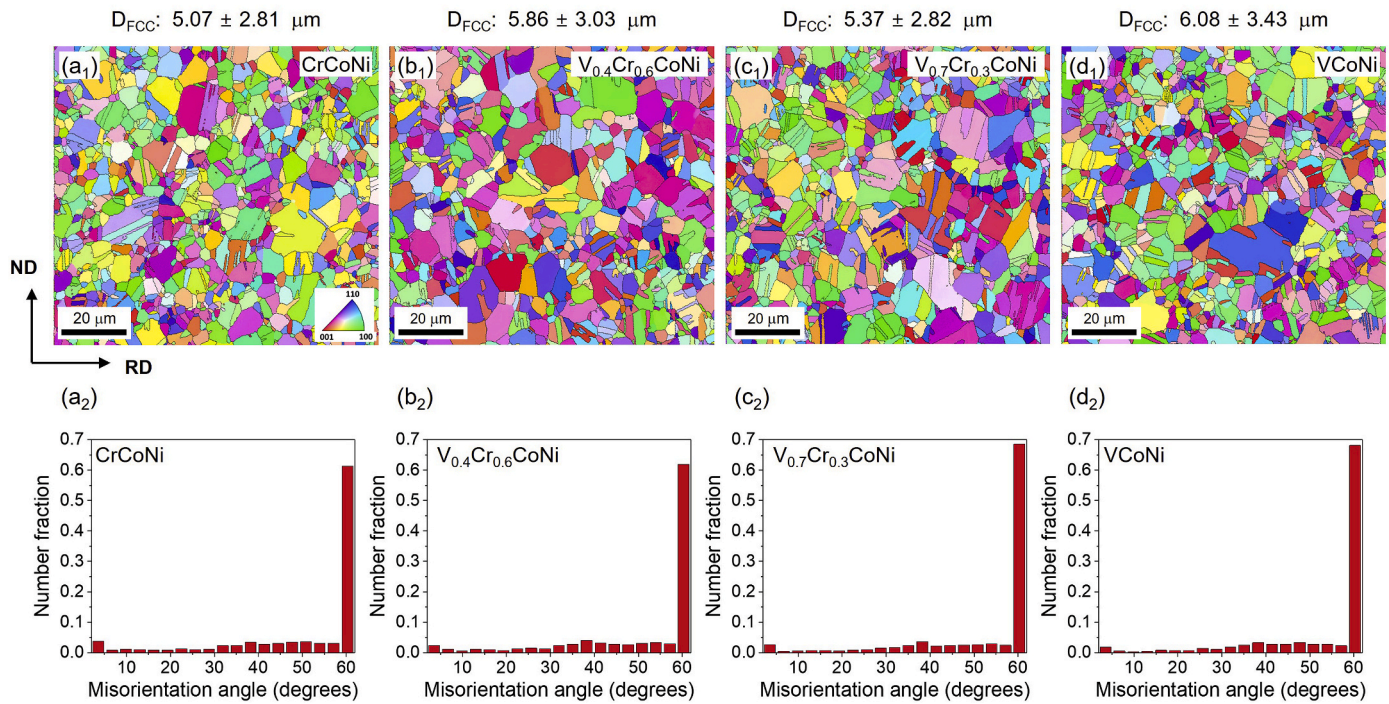
D_{FCC}: 5.07 ± 2.81 μm D_{FCC}: 5.86 ± 3.03 μm D_{FCC}: 5.37 ± 2.82 μm D_{FCC}: 6.08 ± 3.43 μm

Fig. 1. (a_1–d_1) EBSD IPF maps and (a_2–d_2) misorientation angle graphs of the annealed $V_xCr_{1-x}CoNi$ (x = 0, 0.4, 0.7, 1) alloys.

with possessing 0.0007%/MPa of normalized HEI.

3.3. Thermal desorption analysis

To investigate the effects of H content on HE susceptibility, TDA was performed on the H pre-charged alloys. A preliminary analysis was performed by raising the temperature to 800 °C at a heating rate of 400 °C h^{-1} (Fig. S1). This analysis confirmed that none of the alloys exhibited secondary high-temperature peaks. The secondary peaks correspond to irreversible trap sites associated with high activation energy for H desorption and diffusion [40]. Accordingly, only the first peaks representing diffusible H at reversible trap sites were investigated in the temperature range below 400 °C.

As shown in Fig. 3a_1–d_1, the total diffusible H content in the CrCoNi alloy was 13.53 wt ppm, and it increased to 26.48 wt ppm in the VCoNi alloy as the V content increased. The increased V content intensifies lattice distortions and enhances lattice friction stress [26], providing a higher local elastic strain energy and larger lattice space. This variation facilitates H trapping in the lattice, thereby increasing the total H content. The lattice parameter measured from the XRD profiles gradually increased from 3.56 to 3.59 Å in steps of 0.01 Å with increasing V content (Fig. S2). However, V is a representative element with high hydrogen affinity [41]; thus, it can increase the total H content in this VCrCoNi alloy system through both structural and chemical factors for H trapping. A further investigation is required to independently clarify the individual roles in the interactions of H with lattices.

Despite the increase in H content with increasing V content, the HE susceptibility and normalized HEI were lower in VCoNi than in CrCoNi, as shown in Fig. 2. The E_a for H desorption and diffusion calculated based on the Kissinger equation indicated that all the four alloys had almost identical binding energies of approximately 30 kJ mol^{-1} (Fig. 3a_2–d_2). This result suggests that the H in the four alloys possesses a similar degree of interaction with microstructural defects, and analogous thermal and mechanical energies are required for the trapped H to become diffusible beyond the binding energy. During tensile deformation, the applied mechanical energy causes H to diffuse from the reversible trap sites. The similar E_a values also indicate that the effects of

structural and chemical variations caused by V on H trapping are negligible in the initial microstructures before deformation. As the E_a values are comparable in each alloy, it is reasonable to assume that the HE susceptibility depends on the amount of diffusible H and the applied stress [42]. In other words, VCoNi would be the most vulnerable to HE owing to its high H content and flow stress. Nevertheless, as confirmed by the SSRT results, HE susceptibility contradicts the trends, and V70 exhibits the highest resistance to HE, suggesting that additional aspects need to be considered.

3.4. Fractographic observation of SSRT specimens

Fig. 4a–d shows the fracture surfaces after the SSRT tests of the four H pre-charged alloys. The fractures were identified as brittle intergranular fractures at the near surfaces and ductile dimple fractures in the interior. The inset of each image shows enlarged intergranular facets, in which slip bands were developed well. These intergranular fractures result from the synergistic interplay of hydrogen-enhanced localized plasticity (HELP) and hydrogen-enhanced decohesion (HEDE) mechanisms. The depth of the brittle fracture zone (BFZ) was measured as approximately 20 μm and was almost similar in the four alloys. Under identical H pre-charging conditions, the similar depths indicate that the diffusivities of H are comparable to each other, although the total H content increased with the increasing V/Cr ratio. Cracks were also observed on the normal direction (ND) planes of the tensile specimens, which was caused by harsh charging conditions, such as the use of the sulfuric acid solution and high current density (50 mA cm^{-2}) [43].

Fig. 5a–d shows the backscattered electron (BSE) images on the TD plane of the tensile specimens deformed to 30% after H pre-charging. Intergranular cracks were observed in the H-affected BFZ in which deformation substructures were formed. For the V0 alloy, deformation twins were identified as reported by the representative characteristics of CrCoNi alloy owing to its low SFE [20]. Under H-charged conditions, deformation twins are known to serve as the crack propagation sites, usually along incoherent twin boundaries, while they can prevent the propagation depending on their alignment with the crack propagation directions [17]. However, every H-induced crack propagated along the
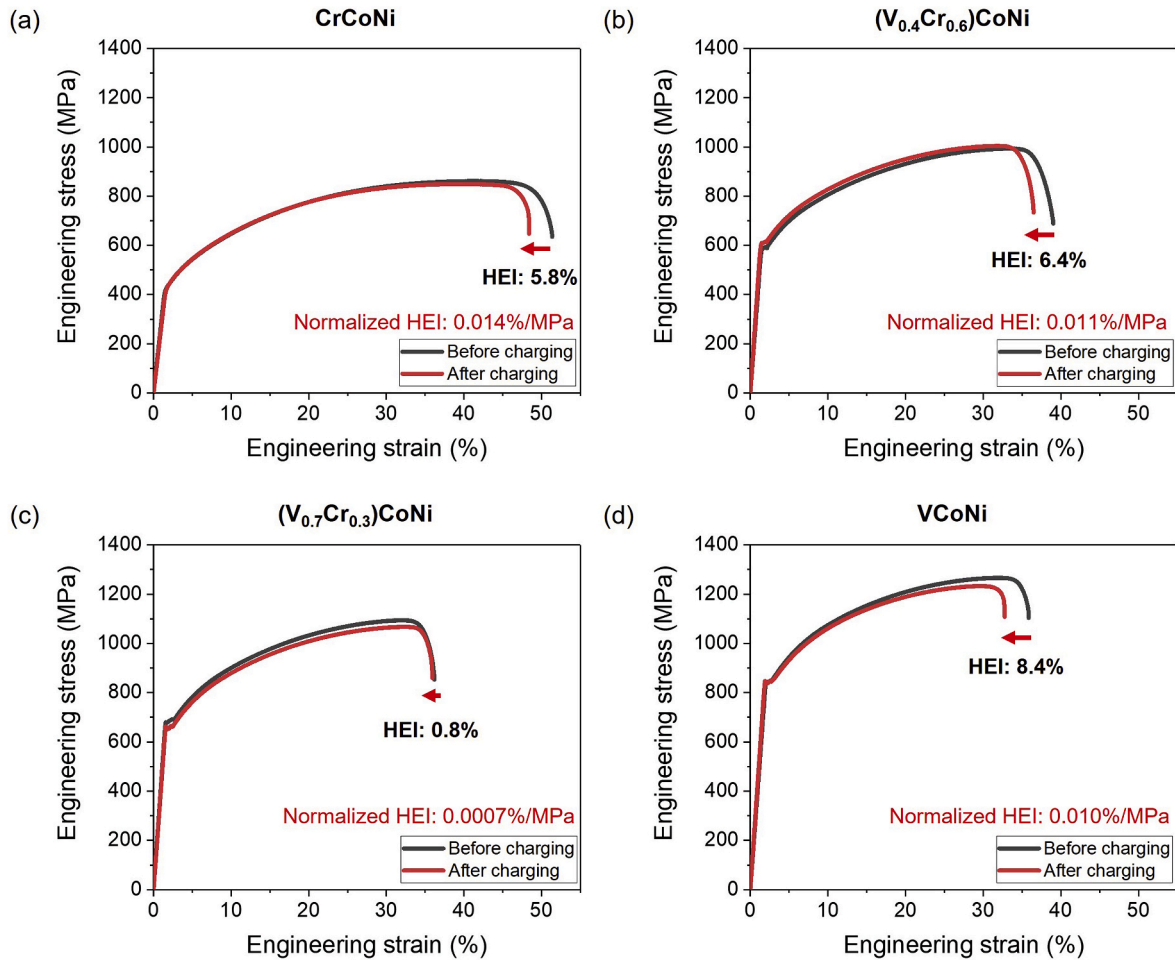
Fig. 2. Engineering stress-strain curves of the SSRT tests before and after cathodic H pre-charging for the annealed (a) CrCoNi, (b) $V_{0.4}Cr_{0.6}$CoNi, (c) $V_{0.7}Cr_{0.3}$CoNi, and (d) VCoNi alloys. The HEI denotes the loss of elongation after cathodic H pre-charging. The normalized HEI indicates the resistance to HE of each alloy by normalizing the HEI to the yield strength.

Table 1
Room-temperature tensile properties of the four alloys before (As) and after (H) cathodic H pre-charging.

Alloy	Specimen	Yield Strength (MPa)	Tensile Strength (MPa)	Elongation (%)
CrCoNi	As	422.2 ± 5.4	860.5 ± 0.6	50.2 ± 2.1
	H	421.5 ± 6.7	838.1 ± 7.2	47.5 ± 1.4
$V_{0.4}Cr_{0.6}$CoNi	As	584.6 ± 3.2	995.3 ± 2.4	39.0 ± 0.1
	H	608.6 ± 2.4	1000.3 ± 5.7	36.4 ± 0.3
$V_{0.7}Cr_{0.3}$CoNi	As	671.5 ± 7.8	1104.0 ± 10.4	35.5 ± 0.5
	H	660.1 ± 15.7	1076.3 ± 13.2	35.3 ± 1.7
VCoNi	As	843.0 ± 0.4	1267.4 ± 1.0	35.4 ± 0.6
	H	839.1 ± 12.5	1239.0 ± 9.2	32.5 ± 0.4

GBs in the V0 alloy in this study. Thus, it is difficult to conclude that twins had a significant role in the crack propagation and HE susceptibility. As the V content increased, twins were not observed, and only dislocation slip bands were predominant near the intergranular cracks, as V enhances the SFE [26]. The slip bands consisted of dislocation network substructures that induce dynamic slip-band refinement effects [19]. Although H pre-charging is known to lower the SFE and alter the deformation behaviors [13–15], twins were not observed even in the V40 alloy, which had the lowest SFE among the V-containing alloys. Thus, it is confirmed that there is no distinct variation in the deformation behaviors after H pre-charging. The observed fracture surfaces

indicate that only intergranular fracture occurs with no transgranular cracks, confirming that the GBs are the predominant sites where H has the highest affinity to interact most actively in the H pre-charged region. Although all four alloys have similar depths of the H-affected BFZs in which only intergranular facets prevail, the HE susceptibility differs, and V70 exhibits the highest resistance to HE with no apparent reduction in tensile ductility. Thus, this observation suggests that directly correlating the BFZ depth with the HE susceptibility is difficult.

3.5. Development of intergranular cracks

As the aforementioned fracture surfaces provided only the terminal results after the fracture occurred, the development of cracks along the GBs according to stepwise tensile strains was investigated for the interrupted SSRT specimens. Fig. 6a₁–d₃ shows the SEM images on the TD planes of each alloy deformed with 10%, 20%, and 30% tensile strains. From these observations, the progress of crack development could be classified into three stages during deformation: (1) the formation of some major cracks, (2) the growth of the major cracks and the formation of new minor cracks, and (3) coalescence and interlinkage.

First, two to three major cracks, indicated by yellow lines in each fractograph, propagated in the depth direction from the surfaces. The cracks had already grown to a depth of more than 15 μm, even at only 10% strain, in all the four alloys (Fig. 6a₁–d₁). These cracks grew rapidly in the H-charged zone, which was measured to be approximately 20 μm (Fig. 4). When they reached the ductile area through further
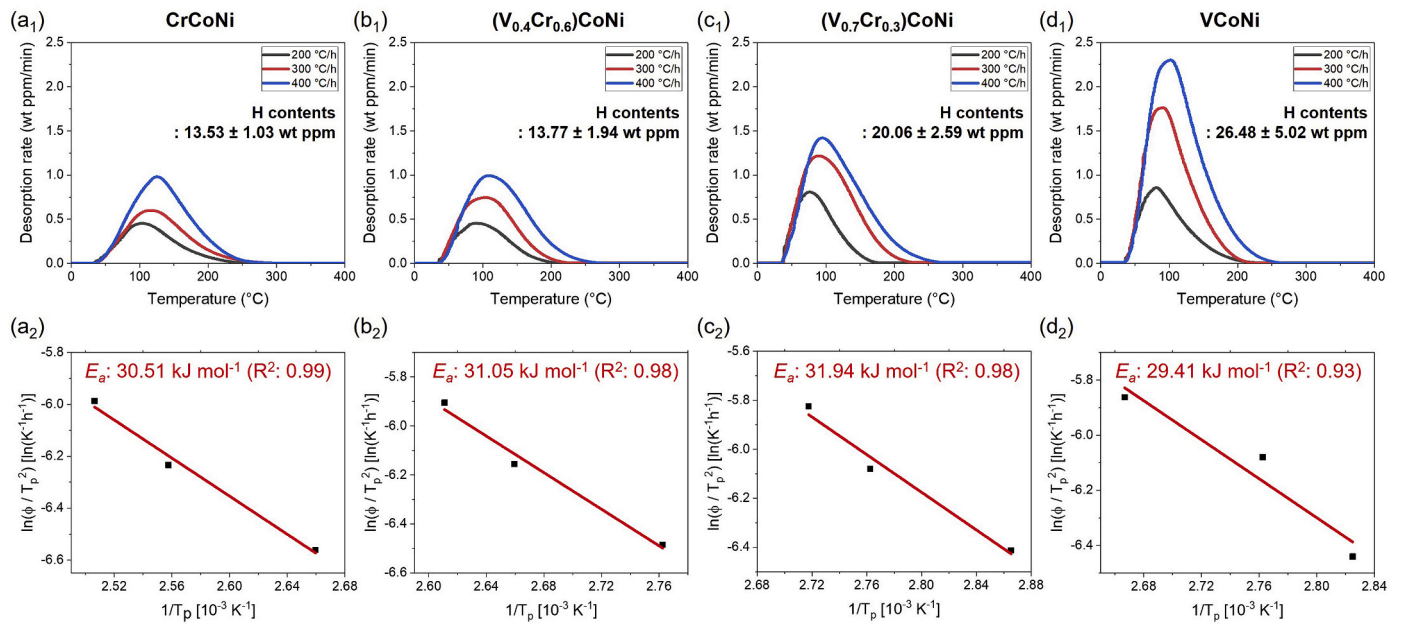
Fig. 3. TDA results. (a$_1$–d$_1$) Desorption rate curves of the V$_x$Cr$_{1-x}$CoNi (x = 0, 0.4, 0.7, 1) alloys at the three heating rates of 200, 300, and 400 °C h^{-1} after cathodic H pre-charging. (a$_2$–d$_2$) Plots of Kissinger equations as a function of peak temperature (T_p) and obtained activation energy (E_a).
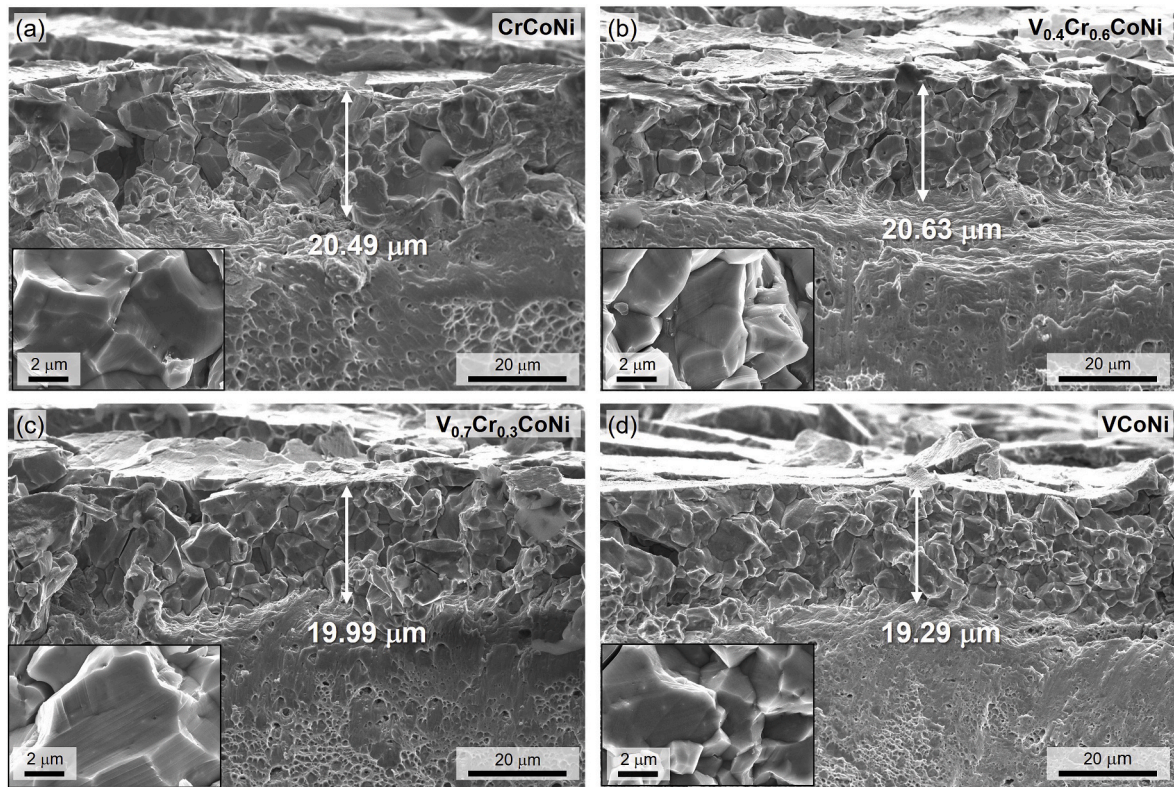

Fig. 4. SEM fractographs of the fractured SSRT specimens for the (a) CrCoNi, (b) V$_{0.4}$Cr$_{0.6}$CoNi, (c) V$_{0.7}$Cr$_{0.3}$CoNi, and (d) VCoNi alloys. The penetration depth, which indicates the H-affected brittle fracture zone, is indicated by white arrows. The inset image shows enlarged intergranular facets.

deformation beyond the H-induced BFZ, propagation no longer occurred, and these cracks widened by forming localized plastic zones at the crack tip (Fig. 6a$_2$–d$_2$) [44]. Second, additional very fine cracks were formed, as indicated by the white arrows in Fig. 6a$_1$–d$_1$. The minor sharp cracks propagated along the GBs and grew in the depth direction owing to the presence of H and the plastic deformation in the region between the major cracks (Fig. 6a$_2$–d$_2$). Both the number density and length

increased with subsequent deformations. These cracks then coalesced and interlinked with each other in the last stage (Fig. 6a$_3$–d$_3$). The minor cracks traveled further in the depth direction and coalesced with other adjacent minor cracks to become major cracks. Finally, the minor cracks and widened major cracks generated large branches in various directions. Notably, the first few major cracks easily grew into the BFZ, even at small strains, indicating that cracks did not begin to form at the
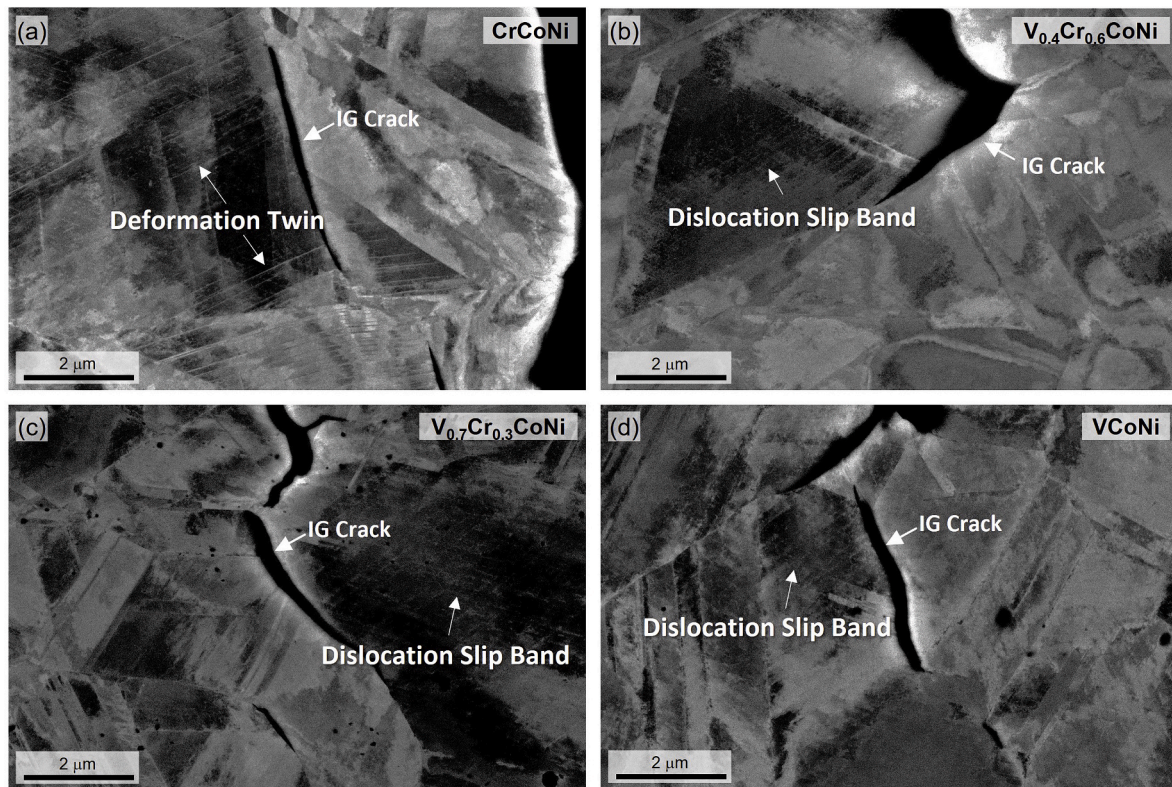
Fig. 5. BSE images showing the deformation behaviors and intergranular cracks for 30%-deformed (a) CrCoNi, (b) $V_{0.4}Cr_{0.6}CoNi$, (c) $V_{0.7}Cr_{0.3}CoNi$, and (d) VCoNi alloys after cathodic H pre-charging.

end of the tensile deformation near the failure strains.

Compared to the V-containing alloys, the applied stress and total H content were the lowest in V0, whereas E_a was almost identical. Thus, the total number of cracks was almost half that in the other alloys. The depth and width of the major cracks continued to increase as the strain increased, whereas new minor cracks were rarely formed (Fig. 6a₁–a₃). However, in the V-containing alloys, the formation of minor cracks was robust, and adjacent cracks were interlinked with each other. The development of major cracks at 10% strain in V40 was markedly similar to that in V0 (Fig. 6b₁). However, at 20% and 30% strains, V40 possessed more newly generated cracks between the major cracks compared with V0. The formation of these minor cracks is attributed to the higher applied stress above the specific critical stress to form new cracks because the total H content was almost identical between V0 and V40 at 13–14 wt ppm. Furthermore, in terms of the deformation behavior of V0, deformation twins formed from the GBs temporarily relieve the applied stress [45]. In other words, the applied strain energy is accommodated inside the grains by the formation of deformation twins in V0. Thus, the total stress applied to the GBs could be reduced, thereby suppressing the formation of intergranular cracks. From the perspective of H content, the twin–twin intersections and dislocation–twin intersections act as hydrogen trap sites [13], which can alleviate H migration by gliding dislocations to GBs and consequently reduce the localization of H and the propensity of intergranular cracking.

V70 underwent a different pattern of crack propagation from V0 and V40. At 30% strain (Fig. 6a₃–c₃), the width of the major cracks of V70 was narrower than that of V40 and V0. Furthermore, more minor cracks were generated between the major cracks at 20% strain, and new cracks continuously formed rather than developing into new major cracks. Numerous sharp minor cracks can be observed in Fig. 6c₃. This result indicates that the high stress applied to V70 mainly formed new minor cracks rather than blunting the major cracks, even though major cracks reached beneath the H-affected BFZ. Furthermore, this difference was

attributed to the higher total H content in V70 than that in V0 and V40. Thus, this effect is most likely to be noticeable in V100 because of its high H content and applied stress; however, a considerable number of minor cracks were already observed at 10% strain (Fig. 6d₁), with apparent linkages between them at 20% strain (Fig. 6d₂). As the strain increased, the development of minor cracks into major cracks and their interlinkages was vigorous, and consequently, crack network structures with mostly major cracks were formed (Fig. 6d₃). In other words, minor cracks remained at 30% strain only in V70, without forming crack interlinkages, which is a unique characteristic among the four alloys.

The observed developments of the major and minor cracks in the four alloys were quantitatively investigated using statistical analysis, as shown in Fig. 7. The number of cracks was determined in the three deformation stages by classifying the two groups based on the crack depth of 5 μm (Fig. 7a), and the proportion of the two groups is indicated in the bar graphs. This plot indicates that the total number of cracks substantially depends on the presence of V in the alloys. The depths and widths of all the cracks were averaged, as shown in Fig. 7b and c, respectively. The number of cracks was significantly smaller at ~100 in V0 than in the V-containing alloys, and the average depth increased rapidly as the strain increased. This result reflects the formation of fewer minor cracks owing to the lower applied stress and total H content. The number of cracks with a depth lower than 5 μm was the largest in V70, in which the average depth reached only ~4 μm, even at 30% strain. V70 maintained the fraction of minor cracks at ~80% despite an increasing amount of deformation. In contrast, the fraction of minor cracks decreased significantly as the strain increased in the other three alloys, indicating the active coalescence and development of minor cracks into major cracks.

The average crack width in Fig. 7c increased as the strain increased in all four alloys. This increase was pronounced in V0, and the average depth of V0 showed a similar trend as well. These results of the average width and depth can be directly related to the evolution of major cracks,
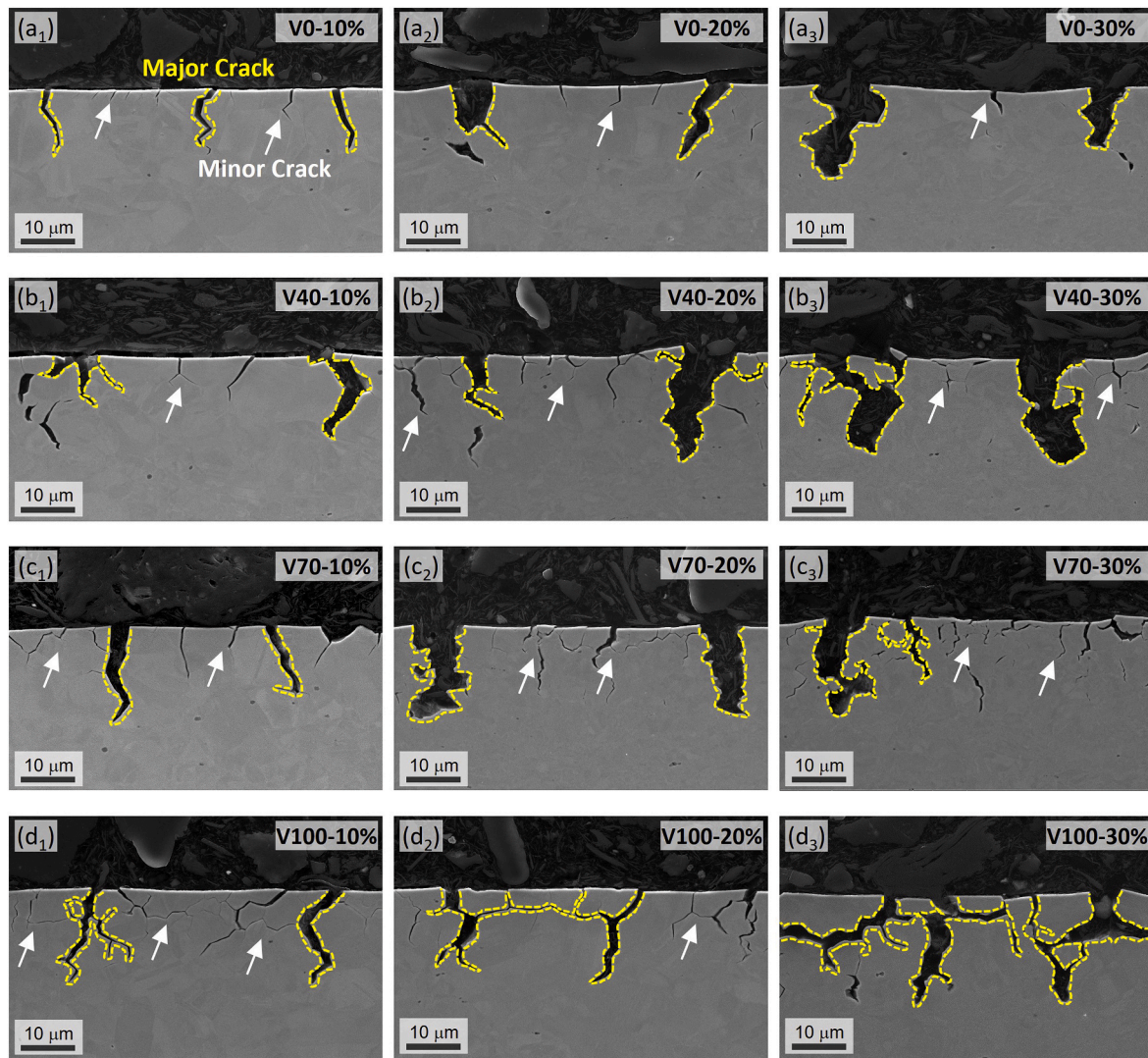
Fig. 6. SEM fractographs on the TD planes of the (a) CrCoNi, (b) $V_{0.4}Cr_{0.6}CoNi$, (c) $V_{0.7}Cr_{0.3}CoNi$, and (d) VCoNi alloys. The subscripts 1, 2, and 3 indicate the tensile strains of 10%, 20%, and 30%, respectively. The major and minor cracks are indicated by yellow dotted lines and white arrows, respectively. (For interpretation of the references to color in this figure legend, the reader is referred to the Web version of this article.)
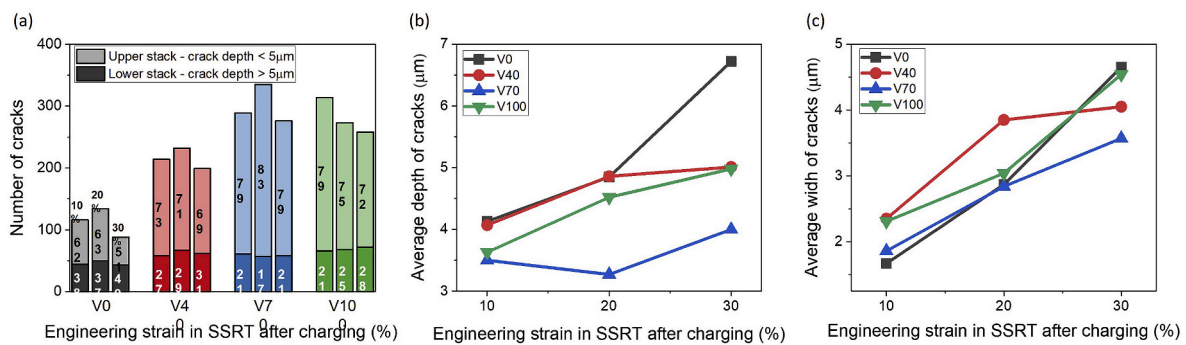

Fig. 7. Statistical results for crack developments corresponding to 10%-, 20%-, and 30%-deformed alloys. (a) A number of cracks and fractions of cracks with depths lower or higher than 5 μm, (b) average depth of cracks, and (c) average width of cracks.

as the propensity of the minor cracks to form and grow is rare. V40 exhibited the largest average width at 20% strain owing to the blunting of major cracks, but a subsequent further increase in the width was alleviated by the formation of new minor cracks after deformation (30%). Interestingly, V70 showed the smallest average width at 30% strain owing to the formation of numerous new cracks, whereas the formation of minor cracks in the early stage and the easy development to major cracks in V100 led to a rapid increase in the width comparable to that in V0.

4. Discussion

Although the HE evaluation through SSRT tests showed an overall decrease in the normalized HEI with increasing V content, V70 exhibited the highest resistance to HE in this study. This discrepancy in HE susceptibility could not be attributed directly to the H content, stress levels, areas of BFZs, or fracture appearance alone. Instead, the progress of intergranular cracks indicated a distinct difference in each alloy, inducing a discrepancy in HE susceptibility. Accordingly, the following sections describe the factor affecting this contrasting propagation (Section 4.1) and how this factor depends on the V content (Section 4.2).

4.1. Resistance to crack propagations according to grain boundary characteristics

In FCC single-phase alloys, H-induced crack propagation occurs primarily at the GBs [12], as confirmed in this study. The distribution and type of GB influence the physicochemical properties of polycrystalline materials, such as corrosion [27], HE [28,29], fatigue [30], creep [31], and liquid metal embrittlement [32]. Among the numerous methods for classifying GBs, CSL boundaries are known to be effective in determining the properties of GBs [46]. Accordingly, GBs are classified into SBs ($\Sigma \leq 29$) or random boundaries ($\Sigma \geq 29$) corresponding to the reciprocal number density (Σ) of the lattice site [47] according to the Brandon criterion [37]. A boundary that contains a high density of lattice points in a CSL is expected to have low energy because of its good atomic fit. Accordingly, owing to the higher cohesion strength than that of random boundaries [48], crack initiation and propagation are more difficult at SBs. Thus, a high fraction of SBs is achieved to obtain desirable properties through GBE. GBE manipulates the structures and properties of GBs through thermomechanical treatment, mostly through repeated cycles of deformation and annealing, to avoid the development of strong recrystallization textures [49]. A successful example of GBE was reported by Bechtle et al. [28], who could alleviate the reduction in tensile ductility and fracture toughness caused by H by adjusting the fraction of SBs in pure Ni.

SBs of low Σ are generally referred to as $\Sigma 3^n$ boundaries generated by the multiple twinning mechanism, in which several twin crystals are aligned by the identical twin law [50]. Annealing twins are representative examples of the $\Sigma 3^n$ boundaries. Multiple twinning occurs most frequently in FCC alloys with a low SFE; *e.g.*, when two $\Sigma 3^n$ boundaries interact, a new boundary is formed, which can only be a $\Sigma 3^n$-related boundary according to the geometrical constraints at the triple junction [49,51]. All four alloys can be classified as twinning materials with comparatively low SFEs owing to the presence of annealing twins in their initial microstructures; these twinning materials are known to be suitable for GBE. However, although specific thermomechanical treatments to utilize GBE were not conducted in this study, intergranular cracks emerged in various morphologies and pathways, as illustrated in Figs. 5 and 6. In this respect, further investigations were focused on these dissimilar developments of intergranular cracks, which could have originated from the differences in the GB properties considering the following factors.

First, the fraction of SBs was considered. In general, although both the length and number fractions can be considered, the number fraction is more widely employed as a standard. The number fraction can appropriately represent the number of potential crack arrest sites, whereas the actual length of the boundaries extending from these locations is of secondary importance [48,52]. In other words, the frequency of cracks that encounter SBs directly correlates with intergranular fracture resistance. In addition to the fraction of SBs, the fraction of STJs is considered another crucial factor. When a triple junction is connected to at least one SB, it is referred to as an STJ [53], which also has the effect of resisting crack propagation. For example, if only one SB encounters a triple junction (J_1), the crack along a random boundary is deflected into another random boundary. Similarly, a crack can be blocked when two SBs exist (J_2). Consequently, the crack cannot reach a triple junction with three SBs (J_3). Thus, higher resistance to intergranular fracture is ensured for a larger fraction of STJs. Additionally, it is critical to ensure the connectivity of the GBs. The most quantitative indicator for the connectivity of GB networks is the distribution of triple junctions [53,54]. As the overall number of STJs increases, the connectivity of the random boundaries decreases, resulting in the isolation of the random boundary cluster. Under these circumstances, the crack cannot propagate indefinitely.

Considering these two factors, the SBs and STJs in the initial microstructure were examined using the Pythorient program (Fig. 8, Table 2). The gradient from white to blue represents the increasing density of the triple junctions. The yellow, red, and black boundaries correspond to the $\Sigma 3$, $\Sigma 9$, and random boundaries, respectively. J_1, J_2, and J_3 are indicated by the green, yellow, and red triangles, respectively. The calculated fractions of the SBs and STJs were nearly identical for V0 and V40. V100 exhibited a similar fraction of SBs, whereas the fraction of STJs was smaller than those of V0 and V40. On the other hand, V70 showed a larger fraction of both SBs and STJs ($\sim$0.46), indicating that SBs and STJs play a critical role in the resistance to the H-induced crack propagations of V70. As shown in Fig. 6, the stress applied to V70 formed new minor cracks rather than blunting the pre-existing major cracks. In addition, unlike in V100, new minor cracks barely converged into major cracks without becoming interconnected. Thus, it is reasonable to assume that this sluggish propagation of new minor cracks (Fig. 6c$_3$), despite sufficient deformation and the high H content in V70, is correlated with a large fraction of SBs and STJs in the initial microstructures.

To directly observe the role of SB and STJ on the crack morphologies and routes, the propagation paths along the GBs in V70 were confirmed by investigating the grain orientations, as shown in Fig. 9. After identifying a region with distinct crack deflection and block (Fig. 9a and b), the orientation analysis of each GB was performed using EBSD to determine the distribution of SBs and STJs. The STJs are indicated by the green, yellow, and red triangles for J_1, J_2, and J_3, respectively. In Fig. 9c, the light orange, black, and blue lines correspond to the intergranular cracks, random boundaries, and SBs, respectively. First, through the orientation analysis of the GBs at the surface, the GBs were classified as $\Sigma 3$ and $\Sigma 25$ boundaries with symmetric misorientations of 60.0° [111] and 51.7° [331], respectively. This indicates that it is difficult for the major cracks to form at the SBs on the surface at the beginning of the deformation. This result also indicates that a larger proportion of SBs may reduce the possibility of intergranular crack initiation.

From the main major crack, propagation is preferred perpendicular to the applied tensile direction or parallel to the ND, thus requiring less mechanical energy. The first branch from the major crack followed a random boundary of 6° and encountered J_1; it chose a random boundary of 56°. In other words, as the bottom GB is $\Sigma 3$ SB (60.0° [111]), the crack traveled along the remaining random boundary at J_1, although the propagation along the bottom direction is preferred in terms of mechanical energy. At J_2 (at the corresponding point indicated in Fig. 9a), the propagated crack along the random boundary of 33° was entirely blocked by the two $\Sigma 3$ SBs. In this series of processes, all the cracks propagated only along the random boundaries. Thus, it can be demonstrated that SBs and STJs affect the development of cracks, and their large proportion in V70 inhibits the interlinkage and further growth of minor cracks into major cracks.

As previously mentioned, both SBs and STJs are attributed to multiple twinning mechanisms, which are further related to TRDs. A TRD represents a grain cluster in which every grain is connected to at least one other grain through a $\Sigma 3^n$-related boundary [55]. In FCC materials, it can be alternatively described as a bundle of recrystallized grains where multiple twinning occurs during annealing. In other words, the grains contained within the TRD are all connected by SBs, and cracks can only propagate along the TRD exterior boundary owing to the unstable energy states. Thus, as the TRD size increases, the number of boundaries
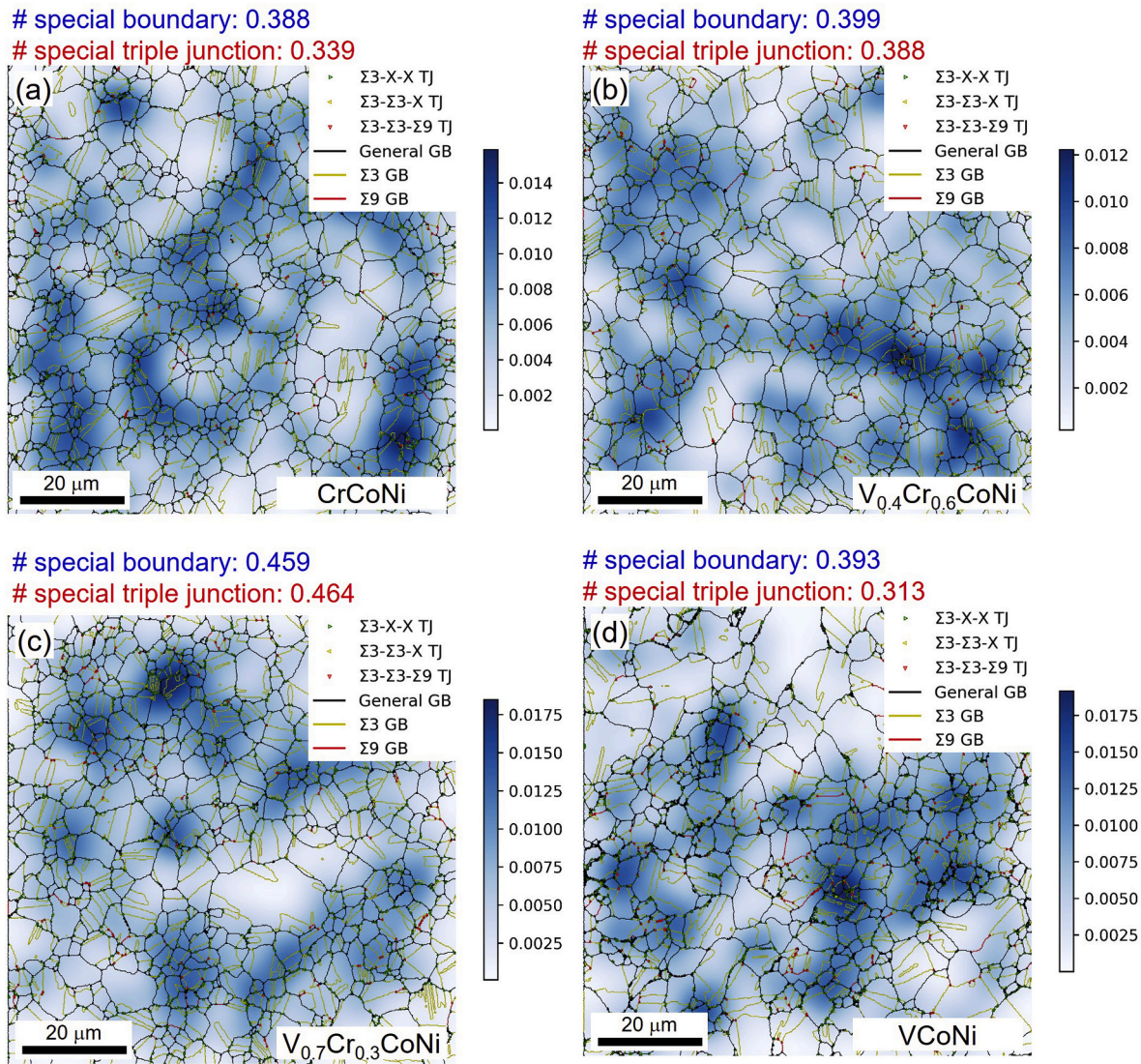
special boundary: 0.388
special triple junction: 0.339

special boundary: 0.399
special triple junction: 0.388

special boundary: 0.459
special triple junction: 0.464

special boundary: 0.393
special triple junction: 0.313

Fig. 8. Triple junction maps obtained using Pythorient for the (a) CrCoNi, (b) $V_{0.4}Cr_{0.6}CoNi$, (c) $V_{0.7}Cr_{0.3}CoNi$, and (d) VCoNi alloys. The gradient from white to blue represents the increasing density of triple junctions. The yellow, red, and black boundaries correspond to the $\Sigma3$, $\Sigma9$, and random boundaries, respectively. J_1, J_2, and J_3 are indicated by the green, yellow, and red triangles, respectively. (For interpretation of the references to color in this figure legend, the reader is referred to the Web version of this article.)

Table 2
Number fraction (#) of the SBs and STJs in the initial microstructure of each alloy.

Alloy	# SBs	Total # STJs	# STJ-J_1	# STJ-J_2	# STJ-J_3
CrCoNi	0.388	0.339	0.307	0.018	0.014
$V_{0.4}Cr_{0.6}CoNi$	0.399	0.388	0.340	0.020	0.028
$V_{0.7}Cr_{0.3}CoNi$	0.459	0.464	0.406	0.022	0.036
VCoNi	0.393	0.313	0.273	0.017	0.023

where crack propagation occurs is reduced, and the susceptibility of intergranular fracture decreases. In this respect, the TRD size can be employed as a significant comprehensive indicator of HE resistance, as it includes the fraction of both SBs and STJs.

Fig. 10 shows the TRD size obtained using the ARPGE program for the initial microstructures, and the results are summarized in Table 3. Each cluster, denoted by a different color, represents a TRD composed of multiple grains. It is surrounded by thick black lines, indicating the exterior boundaries of the TRD. The TRD size of V70 was the largest among the four alloys (Table 3), which is consistent with the values of

SBs and STJs in Table 2. Considering that the TRD size depends on the growth rate and the grain size, the TRD size was normalized to the grain size, although the grain sizes were almost identical. The resulting ratio was also larger in V70 by 6%–16% than that in the remaining alloys (Table 3). In addition, as one of the quantitative values, the average number of grains per TRD (N_g) estimates the multiple twinning capacity [38]. A large N_g value indicates how frequently multiple twinning occurs within the TRD and how easily SBs and STJs are produced. All the factors, including the fraction of SBs and STJs, TRD size, and N_g, were the largest in V70, confirming that these indicators well stand for the high resistance to the HE of V70.

4.2. Origins of initial microstructure with securing the resistance of hydrogen embrittlement

The preceding section discussed the variations in the TRD size and fractions of SBs and STJs according to the V content. Considering that all the TRDs are generated from one crystal lattice orientation and do not coalesce prior to grain growth, the location where the TRD starts to grow corresponds to a recrystallization nucleus [56]. As the distribution of
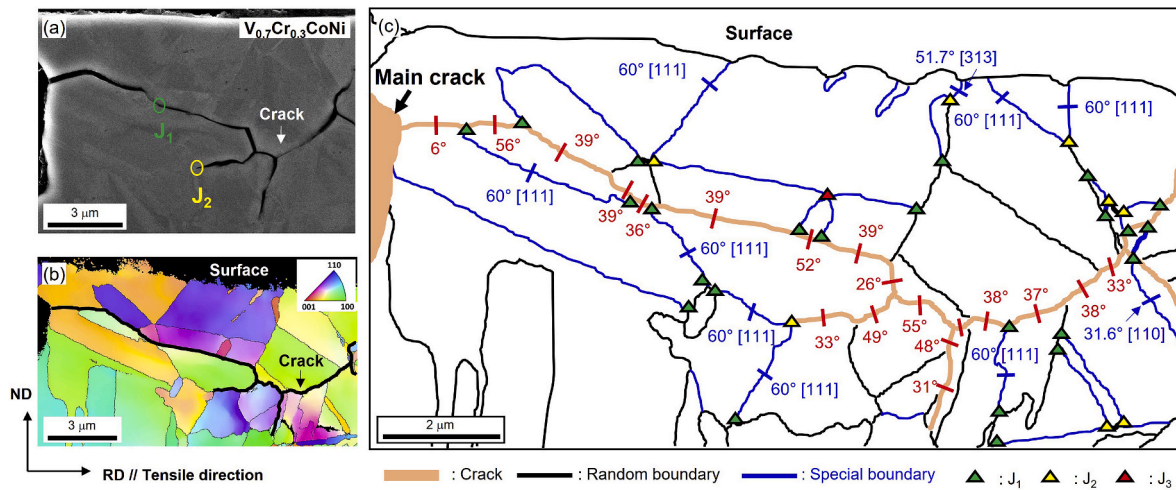
Fig. 9. (a) SEM fractograph, (b) EBSD IPF map, and (c) EBSD grain boundary map of the TD plane in 30%-deformed $(V_{0.7}Cr_{0.3})CoNi$ after cathodic H pre-charging. The angle in (c) indicates the misorientation between two adjacent grains. Special boundaries are marked with the misorientation angle and rotation axis.
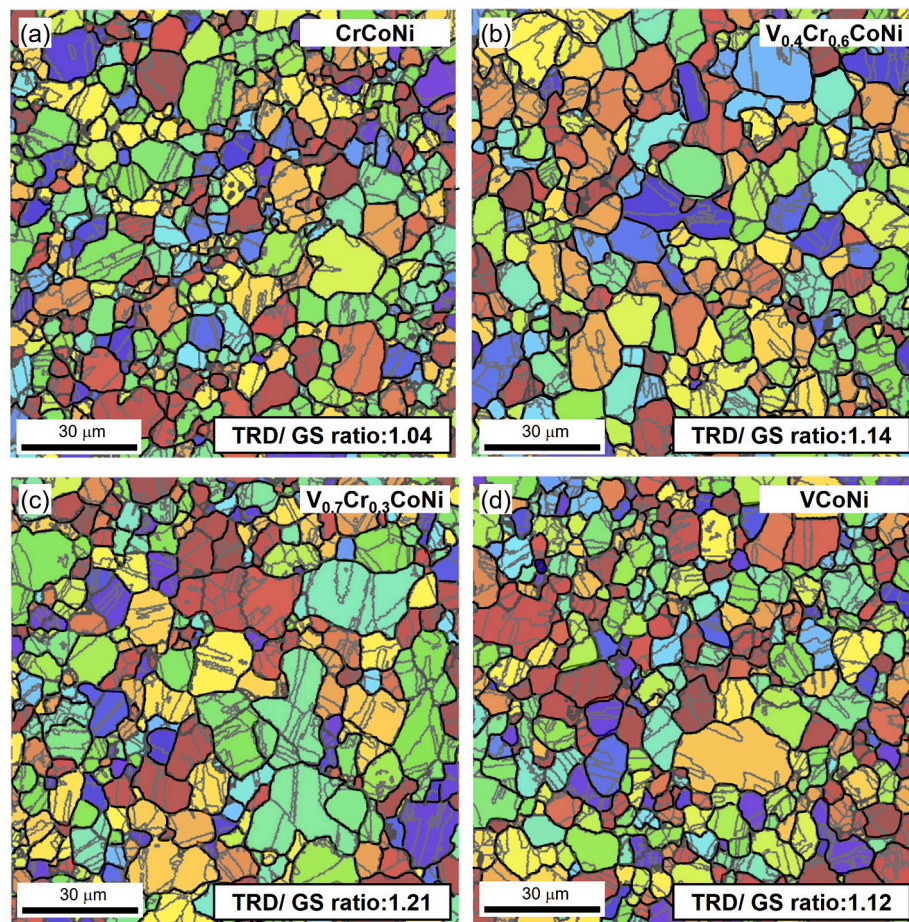

Fig. 10. Reconstructed TRD maps of the EBSD maps in Fig. 1 by using ARPGE software for the (a) CrCoNi, (b) $V_{0.4}Cr_{0.6}CoNi$, (c) $V_{0.7}Cr_{0.3}CoNi$, and (d) VCoNi alloys. The TRD exterior boundaries are indicated by thick black lines. Each cluster composed of several grains is shown with a different color. (For interpretation of the references to color in this figure legend, the reader is referred to the Web version of this article.)

TRDs is directly associated with that of recrystallization nuclei [51], the TRD size is primarily determined by the conditions of the thermomechanical treatment for recrystallization. Several studies have reported that a large TRD size is obtained with a low thickness reduction through cold working, followed by annealing for a short duration [56, 57]. However, the present four alloys were cold-rolled to an identical

thickness reduction of 80% and subsequently annealed at an analogous temperature. Accordingly, unlike the preceding GBE involving repeated cycles of cold working and annealing, the variation in TRD size was not attributed to the thermomechanical processing parameters, but rather it could result from the element effect, V content.

Interestingly, Emeis et al. [34] reported that both solid-solution

Table 3
Results of TRD analysis from ARPGE: 1) TRD size, 2) TRD size/grain size ratio, and 3) the average number of grains per TRD (N_g).

Alloy	TRD size (µm)	TRD size/grain size ratio	N_g
CrCoNi	5.11	1.04	2.29
$V_{0.4}Cr_{0.6}CoNi$	5.73	1.14	2.77
$V_{0.7}Cr_{0.3}CoNi$	6.67	1.21	3.22
VCoNi	6.12	1.12	2.74

strengthening and SFE affect the size of recrystallized grains for Cu–Ni binary alloys subjected to severe plastic deformation and subsequent annealing. In their study, the fluctuation in SFE was not as high as ~12 mJ m^{-2} even with an increase in the Cu content to 50, 65, or 90 at%. However, the $Cu_{50}Ni_{50}$ alloy showed the highest yield strength (referred as a measure of solid-solution strengthening in their study) and the smallest recrystallized grain size at identical homologous temperatures. Pure Cu and Ni metals have comparable yield strengths, but the SFE is much higher, and the recrystallized grain sizes were much larger in pure Ni than in pure Cu at the same homologous temperature. In general, increased solid-solution strengthening and a higher lattice strain field render dislocation movement difficult and lower the mechanical dynamic recovery (MDR) [58]. In contrast, a higher SFE facilitates dislocation climb and cross-slip and promotes dynamic recovery [59]. Dynamic recovery alters the dislocation structures, and the resulting dislocations account for the majority of nucleation sites during recrystallization for metals and alloys in which a significant amount of cold rolling is applied. When MDR is retarded by controlling the solid-solution strengthening and SFE, several retained dislocations directly become numerous nucleation sites, thereby reducing the average TRD size.

Therefore, we hypothesized that the degree of MDR during cold rolling varies with the V content, resulting in different TRD sizes. With increasing V content, the solid-solution strengthening gradually increases, reducing the MDR. According to Chung et al. [26], the electronegativity ($\Delta\kappa$) values of the four alloys increased from 0.1 to 0.156 as the V content increased, and the friction stress gradually increased in the order of 210, 290, 335, and 380 MPa. Calculating the electronegativity of an alloy is an effective method for predicting the solid-solution strengthening [60]. Similarly, the SFE increased as the V content increased. With increasing V content from V0 to V70, the absolute SFE, calculated based on density functional theory, increased significantly in the order of -20, -3, and 27 mJ m^{-2}, whereas it increased only marginally from V70 to V100, *i.e.*, from 27 to 31 mJ m^{-2} [26]. In other words, both solid-solution strengthening and SFE increased as the V content increased, whereas these two factors had opposite effects on the MDR.

To investigate the MDR of the four alloys, the SSRT results with the absent of H pre-charging were analyzed according to the Kocks–Mecking (KM) model [61]. The KM model proposes that the hardening of materials is governed by the competition between dislocation storage and annihilation. In addition, at the end of deformation, a deformation stage with no apparent hardening emerges owing to the equilibrium between hardening and softening. This competitive behavior can be expressed by Eq. (3):

$$\frac{d\rho}{d\varepsilon} = k_1\rho^{1/2} - k_2\rho \tag{3}$$

where the first term on the right-hand side is associated with the athermal storage of dislocations and the second term represents the extent of dynamic recovery. ρ denotes the dislocation density, k_1 is the material constant, and k_2 is the rate of dynamic recovery, which is a function of temperature and strain rate. The first term is proportional to the average distance between dislocations, $\rho^{1/2}$, and refers to the maximum distance that a mobile dislocation can travel, also known as the mean free path. However, as additional obstacles (the spacing of precipitates, grain size,

etc.) can interrupt the movement of dislocations, the KM model assumed that the mean free path is constant [62]. Consequently, the athermal storage rate becomes a constant, K, which is determined by the inverse of the product of the constant mean free path and the magnitude of the Burgers vector, and Eq. (3) can be rewritten as follows:

$$\frac{d\rho}{d\varepsilon} = K - k_2\rho \tag{4}$$

After the differential equation is solved using the work-hardening equation for flow stress (refer to the Appendix in Ref. [63]), Eq. (4) can be modified as follows:

$$\sigma\theta = 0.5k_2\sigma_{sat}^2 - 0.5k_2\sigma^2 \tag{5}$$

where σ and σ_{sat} respectively represent the flow stress and saturated stress at which the stress does not change before necking, *i.e.*, dynamic recovery and work hardening are well balanced [64]. Finally, the rate of dynamic recovery (k_2) can be obtained from the slope ($m = -0.5k_2$) of the curve in Eq. (5); the steeper the slope, the higher the dynamic recovery rate.

Fig. 11a shows the $\sigma\theta - \sigma^2$ plots based on Eq. (5) for the four alloys. The flow stress of the SSRT results was analyzed using the modified Crussard–Jaoul analysis [65]. The modified Crussard–Jaoul analysis based on the Swift equation quantified the strain point at which the transition occurs between multiple deformation stages. Here, stage III before necking corresponds to the region where the MDR is dominated by active cross-slip over the work-hardening effect. Although the deformation stages were divided based on the modified Crussard–Jaoul analysis, the initial region of the plot in Fig. 11a does not exhibit linearity, as it exists in the ambiguous boundary between stages II and III. Nevertheless, the plot quickly settles into a linear region dominated by dynamic recovery. Subsequently, tensile instability occurs and the linearity eventually deviates. The obtained rates of MDR (k_2) were 2.44, 5.74, 6.24, and 5.70 for V0, V40, V70, and V100, respectively, demonstrating that the MDR was most active in V70.

As mentioned above, both solid-solution strengthening and SFE increase as the V content increases, whereas these two factors have opposite effects on the MDR. As schematically illustrated in Fig. 11b, the MDR decreases gradually with a gradual increase in the solid-solution strengthening, whereas the increasing rate of MDR is reduced from V70 to V100 by the marginal increase in SFE. This contrary effect allows the role of solid-solution strengthening in MDR to be more dominant, leading to a lower MDR in V100 than that in V70. Accordingly, V70 possesses the highest active dynamic recovery, the smallest number of nucleation sites before recrystallization, and the largest TRD size. Fig. 12 shows that this large TRD size is directly correlated with the larger fractions of SBs and STJs, increasing the resistance to H-induced crack propagation and interlinkage. After electrolytic H pre-charging and tensile deformation, cracks are initiated at the GBs, particularly at the random boundaries, owing to both the applied stress and H transported by dislocations or pre-decorated at the GBs. When cracks encounter SBs or STJs during propagation, they cannot propagate further. Note that the reduction in the elongation on the stress-strain curves is not caused by an instant brittle fracture from crack initiation but by an acceleration of the plastic instability generated from the development of major cracks and the resulting stress concentrations at the crack tips. In conclusion, as the progression and connection of cracks are postponed, the stress concentration exerted during necking is relatively alleviated, and thus, a high tensile ductility is assured in H pre-charged V70.

5. Conclusions

The research focused on analyzing the resistance to HE of $V_xCr_{1-x}CoNi$ (where x = 0, 0.4, 0.7, and 1) MEAs. Although the overall resistance to HE increased with the V content, interestingly, $V_{0.7}Cr_{0.3}CoNi$ alloy exhibited the highest resistance among the model alloys. The
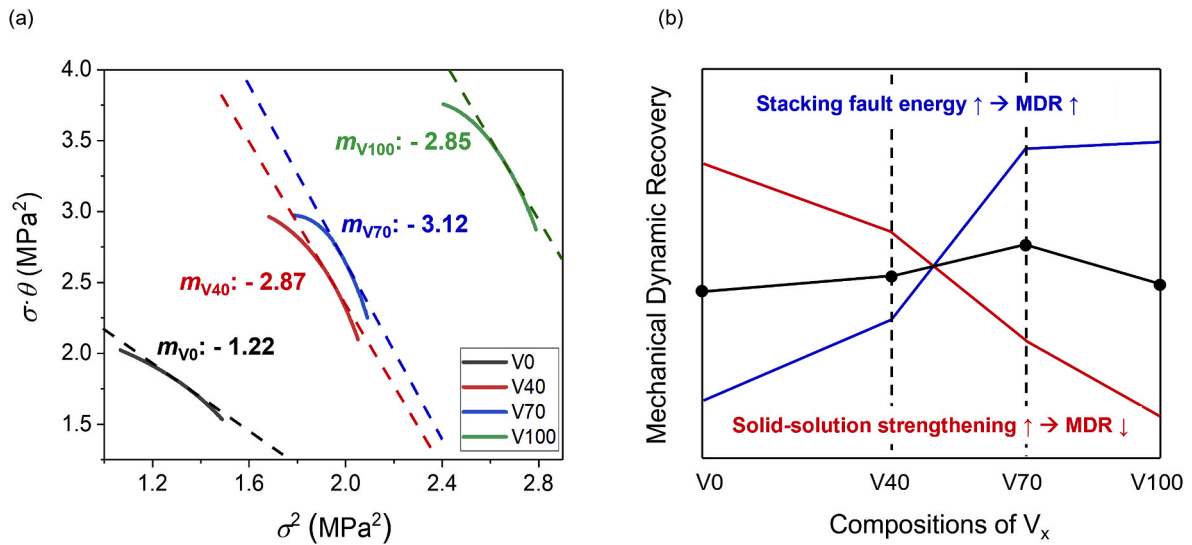
(a)   (b)

Fig. 11. (a) Plots of $\sigma \cdot \theta$ against σ^2 for the four alloys before cathodic H pre-charging according to the Kocks-Mecking model. σ and θ represent the flow stress and the strain-hardening rate from the start point of stage III to necking, respectively. The start point of stage III was obtained from the modified Crussard–Jaoul analysis. The linear portion of the curves determines the dynamic recovery rate (MDR, $k_2 = -2m$). (b) Variations in the MDR by solid-solution strengthening and SFE according to the V content. The red and blue lines indicate the variations in MDR affected by solid-solution strengthening and SFE, respectively. The black line is the summation of the red and blue lines, indicating the total MDR in each alloy after cold-rolling. (For interpretation of the references to color in this figure legend, the reader is referred to the Web version of this article.)
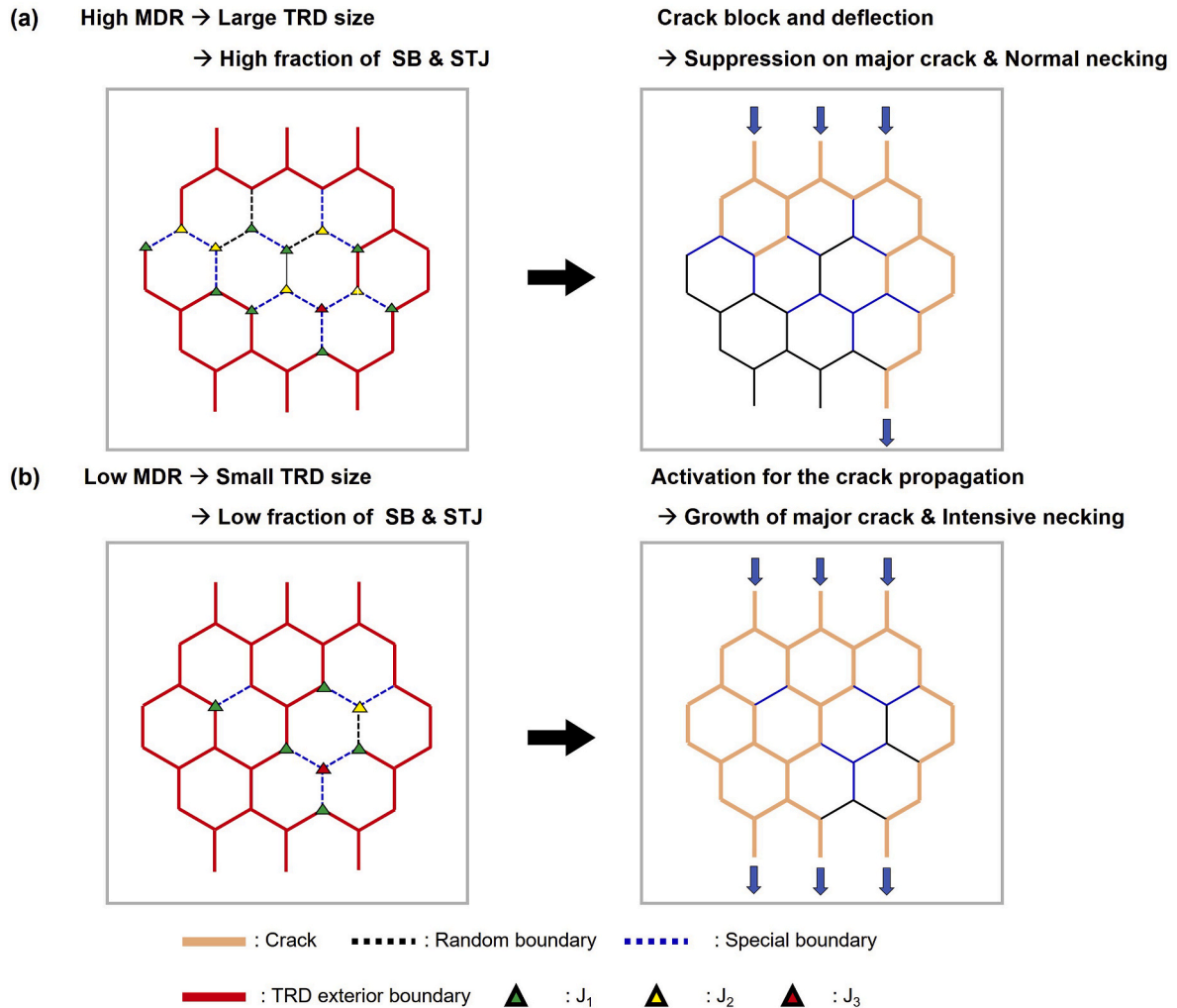

Fig. 12. Schematics of the H-induced crack propagation behaviors of an (a) high-MDR alloy and (b) low-MDR alloy.

underlying mechanisms were discussed in terms of solid-solution strengthening, SFE, and GB characteristics, and the following conclusions were obtained:

(1) The $V_{0.7}Cr_{0.3}CoNi$ showed a deviation from the linear relationship regarding normalized HEI and V content. The discrepancy in HE susceptibility could not be attributed to H content, activation energy, H-induced BFZ areas, fracture appearance, or deformation behaviors.

(2) Interrupted SSRT tests showed that H-induced crack development could be categorized into three stages: (1) major crack formation, (2) growth of major cracks and formation of new minor cracks, and (3) coalescence and interlinkage. However, most of the minor cracks in $V_{0.7}Cr_{0.3}CoNi$ remained without the lack of interlinkages, which prevented the development of major cracks that induced plastic instability.

(3) The analysis of GB characteristics indicated that $V_{0.7}Cr_{0.3}CoNi$ had a larger number fraction of both SBs and STJs than the other alloys. In addition, the TRD size of $V_{0.7}Cr_{0.3}CoNi$ was the largest, consistent with the values of SBs and STJs. Those parameters delayed the crack interlinkage and the growth into major cracks.

(4) The flow stress of the SSRT test, as reinterpreted by the KM model and modified Crussard-Jaoul analysis, revealed that $V_{0.7}Cr_{0.3}CoNi$ had the highest MDR rate. In this MEA system, the effect of V content on solid-solution strengthening and SFE showed opposite trends. The highest MDR of $V_{0.7}Cr_{0.3}CoNi$ was due to the marginal increase in SFE and the gradual decrease in solid-solution strengthening. Finally, the high MDR increased the TRD size and, consequently the fractions of SBs and STJs, resulting in high resistance to crack propagation and HE.

(5) We discovered that the GB characteristics could be influenced by the variation of inherent properties of alloys by manipulating the elemental composition. This strategy could be utilized as a new approach for GB engineering to enhance the resistance to HE. However, in order to optimize the HE resistance of MEA, further studies are required to clarify the correlation between hydrogen and lattice distortion.

CRediT authorship contribution statement

Dae Cheol Yang: Conceptualization, Methodology, Validation, Formal analysis, Investigation, Writing – original draft, Writing – review & editing. **Sang Yoon Song:** Investigation, Methodology, Validation. **Han-Jin Kim:** Investigation. **Sang-In Lee:** Investigation. **Biswanath Dutta:** Supervision, Validation. **Young Kyun Kim:** Methodology, Validation. **Jae-Hyeok Shim:** Supervision, Validation. **Jin-Yoo Suh:** Supervision, Validation. **Young Sang Na:** Supervision, Validation. **Seok Su Sohn:** Project administration, Conceptualization, Visualization, Supervision, Validation, Writing – review & editing.

Declaration of competing interest

The authors declare that they have no known competing financial interests or personal relationships that could have appeared to influence the work reported in this paper.

Data availability

Data will be made available on request.

Acknowledgments

Appendix A. Supplementary data

Supplementary data to this article can be found online at https://doi.org/10.1016/j.msea.2023.145028.

References

[1] M. Aziz, Liquid Hydrogen: a review on liquefaction, storage, transportation, and safety, Energies 14 (18) (2021) 5917, https://doi.org/10.3390/en14185917.

[2] J. von Pezold, L. Lymperakis, J. Neugebauer, Hydrogen-enhanced local plasticity at dilute bulk H concentrations: the role of H–H interactions and the formation of local hydrides, Acta Mater. 59 (2011) 2969–2980, https://doi.org/10.1016/j.actamat.2011.01.037.

[3] M.L. Martin, M. Dadfarnia, A. Nagao, S. Wang, P. Sofronis, Enumeration of the hydrogen-enhanced localized plasticity mechanism for hydrogen embrittlement in structural materials, Acta Mater. 165 (2019) 734–750, https://doi.org/10.1016/j.actamat.2018.12.014.

[4] I.H. Katzarov, A.T. Paxton, Hydrogen embrittlement II. Analysis of hydrogen-enhanced decohesion across (111) planes in α-Fe, Phys. Rev. Mater. 1 (2017), 033603, https://doi.org/10.1103/PhysRevMaterials.1.033603.

[5] M. Hatano, M. Fujinami, K. Arai, H. Fujii, M. Nagumo, Hydrogen embrittlement of austenitic stainless steels revealed by deformation microstructures and strain-induced creation of vacancies, Acta Mater. 67 (2014) 342–353, https://doi.org/10.1016/j.actamat.2013.12.039.

[6] D.S. Bae, U.B. Baek, S.H. Nahm, I. Jo, Effect of electrochemical hydrogen charging time on hydrogen embrittlement of the hot-rolled and accelerated cooling treated API X70 steel, Met. Mater. Int. 28 (2022) 466–474, https://doi.org/10.1007/s12540-021-01082-8.

[7] Y. Qiu, H. Yang, L. Tong, L. Wang, Research progress of cryogenic materials for storage and transportation of liquid hydrogen, Metals 11 (7) (2021) 1101, https://doi.org/10.3390/met11071101.

[8] I.R. Walker, Considerations on the selection of alloys for use in pressure cells at low temperatures, Cryogenics 45 (2005) 87–108, https://doi.org/10.1016/j.cryogenics.2004.05.002.

[9] H. Kobayashi, T. Sano, H. Kobayashi, S. Matsuoka, H. Tsujigami, Current status of evaluation and selecting of materials to be used for hydrogen refueling station equipment in Japan, in: Proceedings of the AMSE 2017 Pressure Vessels and Piping Conference, 2017, pp. PVP2017–55250, https://doi.org/10.1115/PVP2017-66250.

[10] M. Koyama, H. Wang, V.K. Verma, K. Tsuzaki, E. Akiyama, Effects of Mn content and grain size on hydrogen embrittlement susceptibility of face-centered cubic high-entropy alloys, Metall. Mater. Trans. A 51 (2020) 5612–5616, https://doi.org/10.1007/s11661-020-05966-z.

[11] K. Ichii, M. Koyama, C.C. Tasan, K. Tsuzaki, Comparative study of hydrogen embrittlement in stable and metastable high-entropy alloys, Scripta Mater. 150 (2018) 74–77, https://doi.org/10.1016/j.scriptamat.2018.03.003.

[12] B. Kuhr, D. Farkas, I.M. Robertson, Atomistic studies of hydrogen effects on grain boundary structure and deformation response in FCC Ni, Comput. Mater. Sci. 122 (2016) 92–101, https://doi.org/10.1016/j.commatsci.2016.05.014.

[13] M. Koyama, E. Akiyama, K. Tsuzaki, D. Raabe, Hydrogen-assisted failure in a twinning-induced plasticity steel studied under in situ hydrogen charging by electron channeling contrast imaging, Acta Mater. 61 (2013) 4607–4618, https://doi.org/10.1016/j.actamat.2013.04.030.

[14] M. Koyama, S. Okazaki, T. Sawaguchi, K. Tsuzaki, Hydrogen embrittlement susceptibility of Fe-Mn binary alloys with high Mn content: effects of stable and metastable ε-martensite, and Mn concentration, Metall. Mater. Trans. A 47 (2016) 2656–2673, https://doi.org/10.1007/s11661-016-3431-9.

[15] M. Koyama, H. Springer, S.V. Merzlikin, K. Tsuzaki, E. Akiyama, D. Raabe, Hydrogen embrittlement associated with strain localization in a precipitation-hardened Fe–Mn–Al–C light weight austenitic steel, Int. J. Hydrogen Energy 39 (2014) 4634–4646, https://doi.org/10.1016/j.ijhydene.2013.12.171.

[16] H.J. Kim, M.K. Cho, G. Kim, S.Y. Lee, M.G. Jo, H. Kim, J.Y. Suh, J. Lee, Influence of hydrogen absorption on stacking fault energy of a face-centered cubic high entropy alloy, Met. Mater. Int. 28 (2022) 2637–2645, https://doi.org/10.1007/s12540-021-01163-8.

[17] C.K. Soundararajan, H. Luo, D. Raabe, Z. Li, Hydrogen resistance of a 1 GPa strong equiatomic CoCrNi medium entropy alloy, Corrosion Sci. 167 (2020), 108510, https://doi.org/10.1016/j.corsci.2020.108510.

[18] D.C. Yang, Y.H. Jo, Y. Ikeda, F. Körmann, S.S. Sohn, Effects of cryogenic temperature on tensile and impact properties in a medium-entropy VCoNi alloy, J. Mater. Sci. Technol. 90 (2021) 159–167, https://doi.org/10.1016/j.jmst.2021.02.034.

[19] S.S. Sohn, A. Kwiatkowski da Silva, Y. Ikeda, F. Körmann, W. Lu, W.S. Choi, B. Gault, D. Ponge, J. Neugebauer, D. Raabe, Ultrastrong medium-entropy single-phase alloys designed via severe lattice distortion, Adv. Mater. 31 (2019), 1807142, https://doi.org/10.1002/adma.201807142.

[20] G. Laplanche, A. Kostka, C. Reinhart, J. Hunfeld, G. Eggeler, E. George, Reasons for the superior mechanical properties of medium-entropy CrCoNi compared to high-entropy CrMnFeCoNi, Acta Mater. 128 (2017) 292–303, https://doi.org/10.1016/j.actamat.2017.02.036.

[21] B. Gludovatz, A. Hohenwarter, K.V. Thurston, H. Bei, Z. Wu, E.P. George, R. O. Ritchie, Exceptional damage-tolerance of a medium-entropy alloy CrCoNi at cryogenic temperatures, Nat. Commun. 7 (2016), 10602, https://doi.org/10.1038/ncomms10602.

[22] H. Luo, S.S. Sohn, W. Lu, L. Li, X. Li, C.K. Soundararajan, W. Krieger, Z. Li, D. Raabe, A strong and ductile medium-entropy alloy resists hydrogen embrittlement and corrosion, Nat. Commun. 11 (2020) 3081, https://doi.org/10.1038/s41467-020-16791-8.

[23] H. Wang, Z. Hu, J. Cao, S. Zhang, T. Cheng, Q. Wang, Hot deformation and workability of a CrCoNi medium entropy alloy, Met. Mater. Int. 28 (2022) 514–522, https://doi.org/10.1007/s12540-021-01057-9.

[24] X. Zhou, W.A. Curtin, First principles study of the effect of hydrogen in austenitic stainless steels and high entropy alloys, Acta Mater. 200 (2020) 932–942, https://doi.org/10.1016/j.actamat.2020.09.070.

[25] Z. Wu, H. Bei, G.M. Pharr, E.P. George, Temperature dependence of the mechanical properties of equiatomic solid solution alloys with face-centered cubic crystal structures, Acta Mater. 81 (2014) 428–441, https://doi.org/10.1016/j.actamat.2014.08.026.

[26] H. Chung, D.W. Kim, W.J. Cho, H.N. Han, Y. Ikeda, S. Ishibashi, F. Körmann, S. S. Sohn, Effect of solid-solution strengthening on deformation mechanisms and strain hardening in medium-entropy $V_{1-x}Cr_xCoNi$ alloys, J. Mater. Sci. Technol. 108 (2022) 270–280, https://doi.org/10.1016/j.jmst.2021.07.042.

[27] M. Shimada, H. Kokawa, Z.J. Wang, Y.S. Sato, I. Karibe, Optimization of grain boundary character distribution for intergranular corrosion resistant 304 stainless steel by twin-induced grain boundary engineering, Acta Mater. 50 (2002) 2331–2341, https://doi.org/10.1016/S1359-6454(02)00064-2.

[28] S. Bechtle, M. Kumar, B.P. Somerday, M.E. Launey, R.O. Ritchie, Grain-boundary engineering markedly reduces susceptibility to intergranular hydrogen embrittlement in metallic materials, Acta Mater. 57 (2009) 4148–4157, https://doi.org/10.1016/j.actamat.2009.05.012.

[29] Y.J. Kwon, S.-P. Jung, B.-J. Lee, C.S. Lee, Grain boundary engineering approach to improve hydrogen embrittlement resistance in Fe-Mn-C TWIP steel, Int. J. Hydrogen Energy 43 (2018) 10129–10140, https://doi.org/10.1016/j.ijhydene.2018.04.048.

[30] S. Kobayashi, M. Hirata, S. Tsurekawa, T. Watanabe, Grain boundary engineering for control of fatigue crack propagation in austenitic stainless steel, Procedia Eng. 10 (2011) 112–117, https://doi.org/10.1016/j.proeng.2011.04.021.

[31] E.M. Lehockey, G. Palumbo, On the creep behaviour of grain boundary engineered nickel 1, Mater. Sci. Eng., A 237 (1997) 168–172, https://doi.org/10.1016/S0921-5093(97)00126-3.

[32] M.H. Razmpoosh, B. Langelier, E. Marzbanrad, H.S. Zurob, N. Zhou, E. Biro, Atomic-scale investigation of liquid-metal-embrittlement crack-path: revealing mechanism and role of grain boundary chemistry, Acta Mater. 204 (2021), 116519, https://doi.org/10.1016/j.actamat.2020.116519.

[33] F. Emeis, J. Leuthold, K. Spangenberg, M. Peterlechner, G. Wilde, Characterization of special grain boundaries and triple junctions in Cu_xNi_{1-x} alloys upon deformation and annealing, Adv. Eng. Mater. 21 (2019), 1801214, https://doi.org/10.1002/adem.201801214.

[34] F. Emeis, M. Peterlechner, S.V. Divinski, G. Wilde, Grain boundary engineering parameters for ultrafine grained microstructures: proof of principles by a systematic composition variation in the Cu-Ni system, Acta Mater. 150 (2018) 262–272, https://doi.org/10.1016/j.actamat.2018.02.054.

[35] H.E. Kissinger, Reaction kinetics in differential thermal analysis, Anal. Chem. 29 (2002) 1702–1706, https://doi.org/10.1021/ac60131a045.

[36] L. Fournier, D. Delafosse, T. Magnin, Cathodic hydrogen embrittlement in alloy 718, Mater. Sci. Eng., A 269 (1999) 111–119, https://doi.org/10.1016/S0921-5093(99)00167-7.

[37] D.G. Brandon, The structure of high-angle grain boundaries, Acta Metall. 14 (1966) 1479–1484, https://doi.org/10.1016/0001-6160(66)90168-4.

[38] C. Cayron, Quantification of multiple twinning in face-centered cubic materials, Acta Mater. 59 (2011) 252–262, https://doi.org/10.1016/j.actamat.2010.09.029.

[39] S.K. Dwivedi, M. Vishwakarma, Effect of hydrogen in advanced high strength steel materials, Int. J. Hydrogen Energy 44 (2019) 28007–28030, https://doi.org/10.1016/j.ijhydene.2019.08.149.

[40] Y.-C. Lin, I.E. McCarroll, Y.-T. Lin, W.-C. Chung, J.M. Cairney, H.-W. Yen, Hydrogen trapping and desorption of dual precipitates in tempered low-carbon martensitic steel, Acta Mater. 196 (2020) 516–527, https://doi.org/10.1016/j.actamat.2020.06.046.

[41] S. Kumar, A. Jain, T. Ichikawa, Y. Kojima, G.K. Dey, Development of vanadium based hydrogen storage material: a review, Renew. Sustain. Energy Rev. 72 (2017) 791–800, https://doi.org/10.1016/j.rser.2017.01.063.

[42] M. Wang, E. Akiyama, K. Tsuzaki, Hydrogen degradation of a boron-bearing steel with 1050 and 1300MPa strength levels, Scripta Mater. 52 (2005) 403–408, https://doi.org/10.1016/j.scriptamat.2004.10.023.

[43] C. Zheng, G. Yi, Investigating the influence of hydrogen on stress corrosion cracking of 2205 duplex stainless steel in sulfuric acid by electrochemical impedance spectroscopy, Corrosion Rev. 35 (2017) 23–33, https://doi.org/10.1515/corrrev-2016-0060.

[44] X.-K. Zhu, J.A. Joyce, Review of fracture toughness (G, K, J, CTOD, CTOA) testing and standardization, Eng. Fract. Mech. 85 (2012) 1–46, https://doi.org/10.1016/j.engfracmech.2012.02.001.

[45] Q. Huang, Q. Zhu, Y. Chen, M. Gong, J. Li, Z. Zhang, W. Yang, J. Wang, H. Zhou, J. Wang, Twinning-assisted dynamic adjustment of grain boundary mobility, Nat. Commun. 12 (2021) 6695, https://doi.org/10.1038/s41467-021-27002-3.

[46] T. Watanabe, Structural effects on grain boundary segregation, Hardening and Fracture, J. Phys. Colloq. 46 (1985) C4–C555, https://doi.org/10.1051/jphyscol:1985462. –C4-566.

[47] H. Grimmer, W. Bollmann, D.H. Warrington, Coincidence-site lattices and complete pattern-shift in cubic crystals, Acta Crystallogr. A 30 (1974) 197–207, https://doi.org/10.1107/S056773947400043X.

[48] M. Seita, J.P. Hanson, S. Gradecak, M.J. Demkowicz, The dual role of coherent twin boundaries in hydrogen embrittlement, Nat. Commun. 6 (2015) 6164, https://doi.org/10.1038/ncomms7164.

[49] V. Randle, Twinning-related grain boundary engineering, Acta Mater. 52 (2004) 4067–4081, https://doi.org/10.1016/j.actamat.2004.05.031.

[50] C. Cayron, Multiple twinning in cubic crystals: geometric/algebraic study and its application for the identification of the Sigma3(n) grain boundaries, Acta Crystallogr. A 63 (2007) 11–29, https://doi.org/10.1107/S0108767306044291.

[51] V.Y. Gertsman, J.C.H. Henager, Grain boundary junctions in microstructure generated by multiple twinning, Interface Sci. 11 (2003) 403–415, https://doi.org/10.1023/A:1026191810431.

[52] E.M. Lehockey, A.M. Brennenstuhl, I. Thompson, On the relationship between grain boundary connectivity, coincident site lattice boundaries, and intergranular stress corrosion cracking, Corrosion Sci. 46 (2004) 2383–2404, https://doi.org/10.1016/j.corsci.2004.01.019.

[53] M. Kumar, W.E. King, A.J. Schwartz, Modifications to the microstructural topology in f.c.c. materials through thermomechanical processing, Acta Mater. 48 (2000) 2081–2091, https://doi.org/10.1016/S1359-6454(00)00045-8.

[54] V.Y. Gertsman, M. Janecek, K. Tangri, Grain boundary ensembles in polycrystals, Acta Mater. 44 (1996) 2869–2882, https://doi.org/10.1016/1359-6454(95)00396-7.

[55] B.W. Reed, M. Kumar, Mathematical methods for analyzing highly-twinned grain boundary networks, Scripta Mater. 54 (2006) 1029–1033, https://doi.org/10.1016/j.scriptamat.2005.11.045.

[56] D.B. Bober, J. Lind, R.P. Mulay, T.J. Rupert, M. Kumar, The formation and characterization of large twin related domains, Acta Mater. 129 (2017) 500–509, https://doi.org/10.1016/j.actamat.2017.02.051.

[57] S.K. Pradhan, P. Bhuyan, C. Kaithwas, S. Mandal, Strain-annealing based grain boundary engineering to evaluate its sole implication on intergranular corrosion in extra-low carbon type 304L austenitic stainless steel, Metall. Mater. Trans. A 49 (2018) 2817–2831, https://doi.org/10.1007/s11661-018-4608-1.

[58] R.L. Fleischer, Substitutional solution hardening, Acta Metall. 11 (1963) 203–209, https://doi.org/10.1016/0001-6160(63)90213-X.

[59] Y.H. Zhao, Y.T. Zhu, X.Z. Liao, Z. Horita, T.G. Langdon, Tailoring stacking fault energy for high ductility and high strength in ultrafine grained Cu and its alloy, Appl. Phys. Lett. 89 (2006), 121906, https://doi.org/10.1063/1.2356310.

[60] H.S. Oh, S.J. Kim, K. Odbadrakh, W.H. Ryu, K.N. Yoon, S. Mu, F. Kormann, Y. Ikeda, C.C. Tasan, D. Raabe, T. Egami, E.S. Park, Engineering atomic-level complexity in high-entropy and complex concentrated alloys, Nat. Commun. 10 (2019) 2090, https://doi.org/10.1038/s41467-019-10012-7.

[61] H. Mecking, U.F. Kocks, Kinetics of flow and strain-hardening, Acta Metall. 29 (1981) 1865–1875, https://doi.org/10.1016/0001-6160(81)90112-7.

[62] Y. Estrin, H. Mecking, An unified phenomenological description of work-hardening and creep based on one-parameter models, Acta Metall. 32 (1984) 57–70, https://doi.org/10.1016/0001-6160(84)90202-5.

[63] J.J. Jonas, X. Quelennec, L. Jiang, É. Martin, The Avrami kinetics of dynamic recrystallization, Acta Mater. 57 (2009) 2748–2756, https://doi.org/10.1016/j.actamat.2009.02.033.

[64] J.E. Bailey, The dislocation density, flow stress and stored energy in deformed polycrystalline copper, Philos. Mag. A 8 (1963) 223–236, https://doi.org/10.1080/14786436308211120.

[65] B.K. Jha, R. Avtar, V.S. Dwivedi, V. Ramaswamy, Applicability of modified Crussard-Jaoul analysis on the deformation behaviour of dual-phase steels, J. Mater. Sci. Lett. 6 (1987) 891–893, https://doi.org/10.1016/j.msea.2016.12.094.